

Hallmarks of CD8⁺ T cell dysfunction are established within hours of tumor antigen encounter before cell division

Received: 16 August 2022

Accepted: 7 July 2023

Published online: 3 August 2023

Michael W. Rudloff¹, Paul Zumbo^{2,3}, Natalie R. Favret¹, Jessica J. Roetman¹, Carlos R. Detrés Román¹, Megan M. Erwin¹, Kristen A. Murray¹, Sriya T. Jonnakuti¹, Friederike Dündar^{1,2,3}, Doron Betel¹ & Mary Philip^{1,6,7} 

 Check for updates

Tumor-specific CD8⁺ T cells (TST) in patients with cancer are dysfunctional and unable to halt cancer progression. TST dysfunction, also known as exhaustion, is thought to be driven by chronic T cell antigen receptor (TCR) stimulation over days to weeks. However, we know little about the interplay between CD8⁺ T cell function, cell division and epigenetic remodeling within hours of activation. Here, we assessed early CD8⁺ T cell differentiation, cell division, chromatin accessibility and transcription in tumor-bearing mice and acutely infected mice. Surprisingly, despite robust activation and proliferation, TST had near complete effector function impairment even before undergoing cell division and had acquired hallmark chromatin accessibility features previously associated with later dysfunction/exhaustion. Moreover, continued tumor/antigen exposure drove progressive epigenetic remodeling, ‘imprinting’ the dysfunctional state. Our study reveals the rapid divergence of T cell fate choice before cell division in the context of tumors versus infection.

CD8⁺ T cell differentiation during acute infection has been well characterized: naive CD8⁺ T cells encountering cognate antigen are activated, proliferate and undergo clonal expansion, and acquire the ability to produce effector cytokines (interferon (IFN)- γ , tumor necrosis factor (TNF)) and cytolytic molecules (granzyme B (GZMB), perforin 1 (PRF1))¹. During chronic infection, CD8⁺ T cells similarly undergo clonal expansion and initially acquire effector function, but with persistent antigen stimulation, undergo hierarchical loss of effector function and proliferative capacity, upregulate inhibitory receptors (for example, PD-1 and LAG3), and become exhausted². TST found in progressing tumors also lack effector function and express inhibitory receptors;

this dysfunction/exhaustion has been attributed to persistent exposure to tumor antigen and the immunosuppressive tumor microenvironment over days to weeks. We and others have since demonstrated that T cell dysfunction can be observed within a few days of tumor antigen encounter^{3–5}. However, the precise kinetics of how TST are activated, lose effector function and first acquire epigenetic features of dysfunction/exhaustion is not known and has not been assessed *in vivo*.

In metazoans, proliferation and differentiation must be carefully regulated during embryogenesis and throughout life to ensure adequate cell numbers and organ function⁶. In immune cells such as developing thymocytes⁷, helper T cells⁸ and B cells^{9,10}, proliferation

¹Department of Medicine, Division of Hematology and Oncology, Department of Pathology, Microbiology, and Immunology, Vanderbilt School of Medicine, Nashville, TN, USA. ²Department of Physiology and Biophysics, Weill Cornell Medicine, New York, NY, USA. ³Applied Bioinformatics Core, Weill Cornell Medicine, New York, NY, USA. ⁴Institute for Computational Biomedicine, Weill Cornell Medicine, New York, NY, USA. ⁵Division of Hematology and Medical Oncology, Department of Medicine, Weill Cornell Medicine, New York, NY, USA. ⁶Vanderbilt Center for Immunobiology, Vanderbilt University Medical Center, Nashville, TN, USA. ⁷Vanderbilt-Ingram Cancer Center, Vanderbilt University Medical Center, Nashville, TN, USA.  e-mail: mary.philip@vumc.org

has been shown to be required for differentiation to proceed. During acute infection, 24 h of antigen stimulation is sufficient to set CD8⁺ T cells on an antigen-independent proliferation and differentiation path to functional effector and memory states^{11–13}. This ‘autopilot’ differentiation¹⁴ suggests that the initial 24 h after activation is a critical window in which CD8⁺ T cell fate is determined. However, it is unknown whether a similar autopilot differentiation occurs in tumors, driving T cells into a dysfunctional state.

To address this question, we utilized our established autochthonous model of liver carcinogenesis, in which TST can be tracked longitudinally over hours, days and weeks during tumor development¹⁵. We previously identified critical features of tumor-induced CD8⁺ T cell dysfunction/exhaustion (reviewed in ref. 16) in this model, including transcription factor (TF) expression changes such as TCF1 downregulation and TOX upregulation, inhibitory receptor expression (PD-1, LAG3, CD39) and dysfunction/exhaustion-associated epigenetic and transcriptional hallmarks^{5,17}. Therefore, we leveraged our ability to track TST division and differentiation with temporal precision in tumor-bearing hosts. We found that CD8⁺ T cells activated in mice with established liver tumors underwent similar rapid activation and proliferation to T cells during acute infection. However, CD8⁺ T cells activated in tumor-bearing hosts were severely functionally impaired within 24 h of activation, challenging the paradigm that chronic stimulation over days drives TST dysfunction. In contrast, CD8⁺ T cells activated in infected mice could make effector cytokines and cytolytic molecules even before cell division. Furthermore, even fully functional committed effector CD8⁺ T cells rapidly lost cytokine and cytotoxic function upon transfer into mice with liver tumors, demonstrating that negative regulatory signals in tumor-bearing hosts can override functional programming. We made similar findings in a pulmonary metastatic melanoma model with CD8⁺ T cells of different antigen specificity, demonstrating that the impact of the late-stage tumors is not dependent on the tumor origin, tissue or antigen specificity.

We profiled transcriptional and chromatin accessibility changes in CD8⁺ T cells activated in infected mice or tumor-bearing mice at early pre-division time points. Congruous with our functional and immunophenotypic assessment, within 24 h of activation in tumors, TST had acquired epigenetic hallmarks previously associated with later-stage dysfunction/exhaustion. We removed TST from tumors after increasing intervals of initial tumor exposure and assessed function and chromatin accessibility after parking in tumor-free/antigen-free hosts. With increasing initial tumor exposure time, TST had greater retention of tumor-associated/dysfunction-associated chromatin accessibility features. Our studies demonstrate that TST acquire dysfunctional hallmarks, including chromatin accessibility changes, within hours of activation in late-stage tumor-bearing hosts, even before undergoing cell division, with dysfunction hallmarks and epigenetic programs stabilized/imprinted with continued tumor/antigen exposure.

Results

Tumor-specific T cells robustly activate/proliferate but lack effector function

To determine the relationship between proliferation and differentiation to the functional or dysfunctional state, we labeled naive SV40 large T antigen (TAG)-specific CD8⁺ T cells (T cell antigen receptor (TCR)_{TAG}) with carboxyfluorescein succinimidyl ester (CFSE), allowing cell division tracking, and transferred them into mice with TAG-driven liver tumors (ASTxAlb-Cre), or into TAG epitope-expressing *Listeria monocytogenes* (LM_{TAG})-infected C57BL/6 mice (B6; Fig. 1a). We analyzed TCR_{TAG} 12, 36, 48 and 60 h after transfer to capture T cells at all stages of division (Fig. 1b). T cells in both tumor-bearing (T) and infected hosts (E) underwent remarkably robust cell division (6+ divisions within 60 h; Fig. 1b,c), expanded (Extended Data Fig. 1b) and upregulated activation markers CD69 and CD44 (Extended Data Fig. 1a and Fig. 1b). Both E-TCR_{TAG} and T-TCR_{TAG} upregulated LAG3 and PD-1,

reflecting active TCR signaling^{18,19} (Fig. 1b and Extended Data Fig. 1a). T-TCR_{TAG} in tumors, tumor-draining lymph nodes and spleens of ASTxAlb-Cre hosts showed similar proliferation and immunophenotypic changes (Extended Data Fig. 1a). Surprisingly, despite robust activation and proliferation, T-TCR_{TAG} completely failed to produce IFN-γ and TNF in response to TAG peptide restimulation ex vivo; this failure was observed as early as division 1 (Fig. 1d,e and Extended Data Fig. 1c,e). This was in sharp contrast to E-TCR_{TAG} from livers or spleens of infected mice, which produced effector cytokines (IFN-γ/TNF) and cytolytic molecules (GZMB/PRF1) and were capable of degranulation (CD107a membrane localization) within a few cell divisions (Fig. 1d,e and Extended Data Fig. 1c–e). Thus, tumor antigen encounter drove CD8⁺ T cell activation and proliferation without gain of effector function.

Tumor-specific T cell effector function impairment begins before cell division

Given that TST effector function impairment was apparent within a few cell divisions, we next assessed differentiation following activation before cell division (6 h, 12 h, 18 h; Fig. 2a). T-TCR_{TAG} were activated within 6 h with similar kinetics as in infected mice, evidenced by CD69 induction and upregulation of CD44, LAG3 and PD-1 (Fig. 2b and Extended Data Fig. 2a). While E-TCR_{TAG} produced effector cytokines at these early time points, T-TCR_{TAG} showed loss of TNF and failure to induce IFN-γ within 6 h, with near total failure to produce both cytokines by 12 h (Fig. 2c,d and Extended Data Fig. 2c). T-TCR_{TAG} also failed to produce GZMB (Fig. 2d and Extended Data Fig. 2b). Thus, multiple arms of effector function were impaired in TST within hours of activation as compared to infection-activated T cells. Interestingly, TOX, a DNA-binding protein shown to be associated with dysfunction in tumors and exhaustion in chronic viral infection^{16,17}, was not induced at these early time points (Fig. 2e), confirming that TOX does not mediate effector function impairment¹⁷.

Effector CD8⁺ T cells rapidly lose function in tumors

To rule out the possibility that rapid dysfunction in tumors is due solely to inadequate priming, we tested whether committed effector T cells would succumb to tumor-induced dysfunction with kinetics similarly to naive T cells. We adoptively transferred CFSE-labeled day 5 effector TCR_{TAG} (E5d) from LM_{TAG}-infected B6 mice into tumor-bearing ASTxAlb-Cre (E → T) mice or time-matched LM_{TAG}-infected B6 (E → E) mice and analyzed 12 h, 36 h and 7 d later (Fig. 3a). E → E reexpressed CD127 (IL7R; Fig. 3b) and remained IFN-γ/TNF double producers in the liver (Fig. 3c,d) and spleen of secondary recipients (Extended Data Fig. 3a,b), demonstrating that E5d were committed functional effectors that underwent memory differentiation and were not negatively impacted by trafficking to the liver microenvironment. In contrast, E → T proliferated after transfer but began losing cytokine production capacity within 12 h, with complete loss by 7 d (Fig. 3b–d). E → T exhibited the classical hierarchical progression of dysfunction/exhaustion²⁰, with loss of TNF first, followed by IFN-γ (Fig. 3c and Extended Data Fig. 3c). Remarkably, nearly all the effector function loss occurred before cell division (Extended Data Fig. 3c,d), demonstrating again that cell division is not needed to disable effector function.

Tumor-specific T cell dysfunction kinetics in mice with metastatic melanoma

To test whether the rapid loss of TST effector function occurred in other cancer types/tissues with distinct antigen specificity, we utilized a pulmonary melanoma metastasis model. Metastases were induced in B6 mice through intravenous injection of B16 murine melanoma cells expressing the CD8⁺ T cell-recognized ovalbumin_{257–264} epitope fused to EGFP (B16-OVA). Naive OVA-specific TCR transgenic CD8⁺ T cells (TCR_{OTI}) were adoptively transferred into B16-OVA-bearing or LM_{OVA}-infected B6 and analyzed 16 h and 48 h later (Fig. 4a). T-TCR_{OTI} and E-TCR_{OTI} were rapidly activated as evidenced by CD69 and PD-1

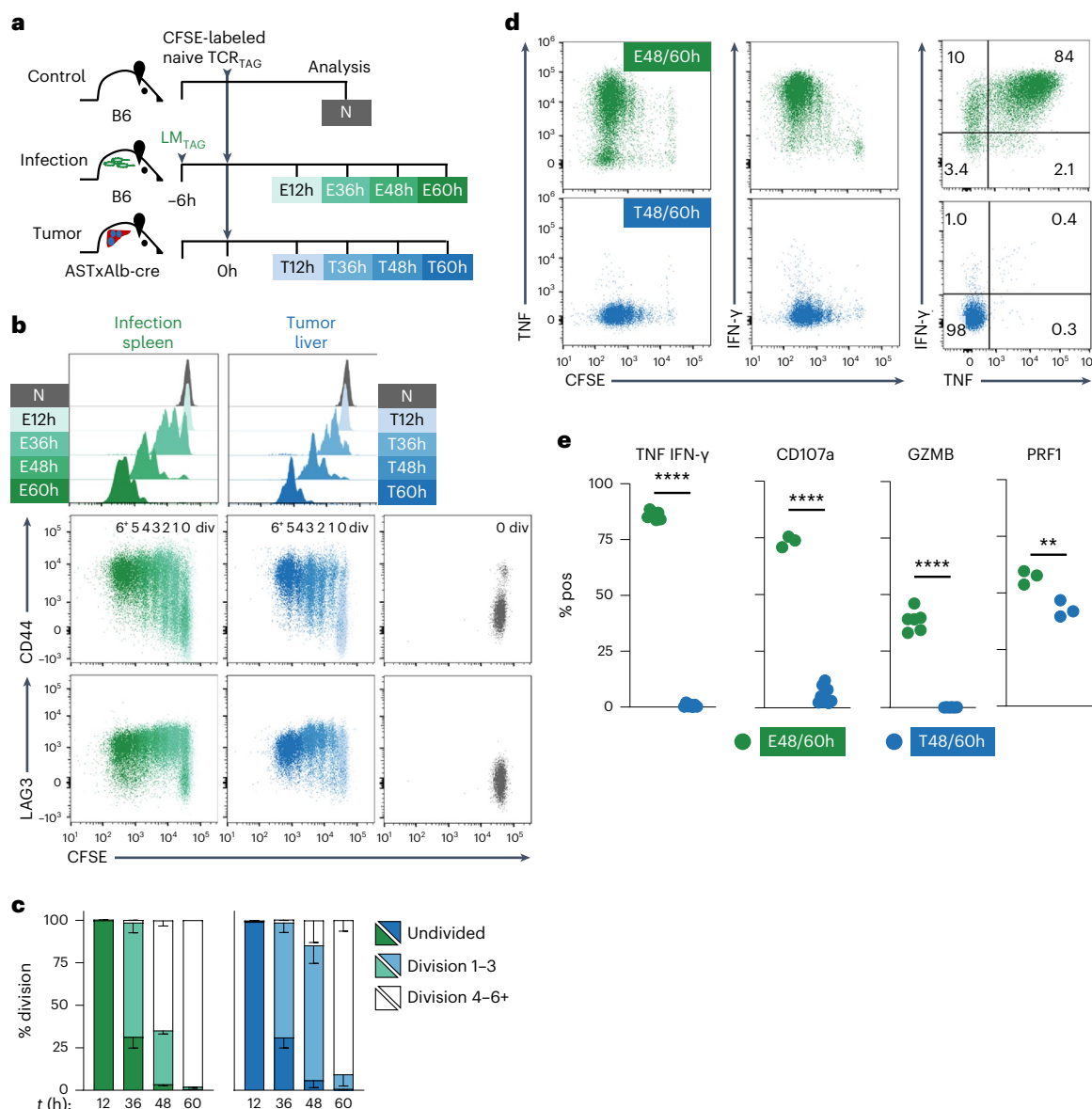


Fig. 1 | Tumor-specific T cells undergo robust activation and proliferation but do not gain effector function. **a**, Experimental scheme: CFSE-labeled naive TCR_{TAG} (Thy1.1) were adoptively transferred into B6 (Thy1.2), LM_{TAG} -infected B6 (Thy1.2) or ASTxAlb-Cre (Thy1.2) mice bearing late-stage liver tumors. TCR_{TAG} were re-isolated at 12 h, 36 h, 48 h and 60 h from infected spleen or tumor livers for flow cytometric analysis (naive in vivo (N; gray); effector (E; green); tumor (T; blue)). **b**, TCR_{TAG} CFSE dilution was assessed at each time point (upper) with CD44 and LAG3 versus CFSE dilution at all time points (lower) shown in comparison to N. All flow plots were gated on live CD8^+ Thy1.1 $^+$ TCR_{TAG} , and data for each time point were concatenated from 3–4 biologic replicates. **c**, Summary plot showing the percentage of cells that were undivided, completed 1–3 cell divisions or 3–6+ cell divisions in infected mice (spleens; green) or tumor-bearing mice (livers; blue) at indicated time points with $n = 3$ mice per group. Error bars represent the standard deviation. Three independent experiments were performed. **d**, TCR_{TAG} IFN- γ and TNF production after 4 h ex vivo TAG peptide stimulation, assessed by flow cytometry. Inset numbers represent the percentage of population in each gate. Gates were set based on no peptide stimulation controls; see Extended Data Fig. 1e for representative figure. **e**, Percentage of TNF $^+$ IFN- γ $^+$ and CD107a $^+$ CD8 $^+$ T hy1.1 $^+$ TCR_{TAG} (E48/60 h and T48/60 h) following ex vivo TAG peptide stimulation, and GZMB and PRF1 expression immediately ex vivo. Each symbol represents an individual mouse, $n = 3$ –9 pooled from two independent experiments.

blue) at indicated time points with $n = 3$ mice per group. Error bars represent the standard deviation. Three independent experiments were performed. **d**, TCR_{TAG} IFN- γ and TNF production after 4 h ex vivo TAG peptide stimulation, assessed by flow cytometry. Inset numbers represent the percentage of population in each gate. Gates were set based on no peptide stimulation controls; see Extended Data Fig. 1e for representative figure. **e**, Percentage of TNF $^+$ IFN- γ $^+$ and CD107a $^+$ CD8 $^+$ T hy1.1 $^+$ TCR_{TAG} (E48/60 h and T48/60 h) following ex vivo TAG peptide stimulation, and GZMB and PRF1 expression immediately ex vivo. Each symbol represents an individual mouse, $n = 3$ –9 pooled from two independent experiments.

** $P = 0.0066$, **** $P < 0.0001$ determined using an unpaired two-tailed Student's *t*-test.

induction before first cell division (Extended Data Fig. 4a,b). At 48 h, both T- TCR_{OTI} and E- TCR_{OTI} proliferated robustly and upregulated CD44 and LAG3 (Fig. 4b). Despite proliferating, T- TCR_{OTI} failed to make TNF and IFN- γ (Fig. 4c,d) and only produced minimal GZMB (Fig. 4d). In marked contrast, E- TCR_{OTI} produced TNF, IFN- γ and GZMB by 16 h following activation and became more functional with time (Fig. 4c,d and Extended Data Fig. 4c).

We next tested whether committed OVA-specific effector T cells would lose function in hosts with pulmonary melanoma metastases.

We adoptively transferred CFSE-labeled day 5 effector TCR_{OTI} (E5d) from LM_{OVA} -infected B6 mice and adoptively transferred them into time-matched LM_{OVA} -infected mice (E \rightarrow E) or B6 mice with established pulmonary B16-OVA metastases (E \rightarrow T; Fig. 4e). Within 24 h following transfer, when the majority of the population had not yet divided (Extended Data Fig. 4d), E \rightarrow T- TCR_{OTI} began losing the ability to produce TNF and IFN- γ , in contrast to E \rightarrow E- TCR_{OTI} , which remained highly functional (Fig. 4f,g). These findings suggest that the rapid onset of TST dysfunction is not specific to the liver microenvironment or liver

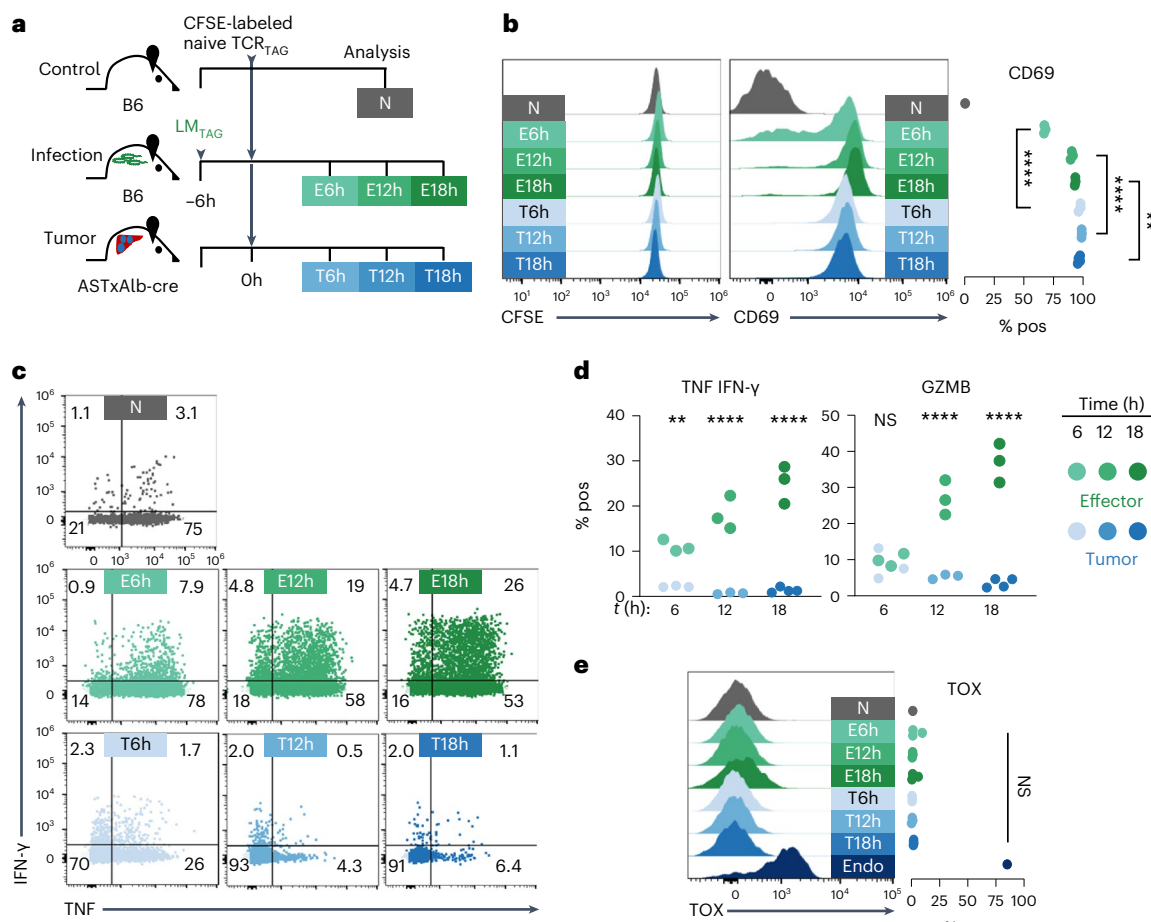


Fig. 2 | Tumor-induced effector function impairment begins before cell division. **a**, Experimental scheme: CFSE-labeled naïve TCR_{TAG} (Thy1.1) were adoptively transferred into B6 (Thy1.2), LM_{TAG}-infected B6 (Thy1.2) or ASTxAlb-Cre (Thy1.2) mice, and lymphocytes were re-isolated from tumor livers (blue) and infected spleens (green) at 6 h, 12 h and 18 h after transfer for analysis by flow cytometry. **b**, Representative histograms of live CD8⁺ Thy1.1⁺ TCR_{TAG} CFSE dilution at each time point (left) and histograms and summary plot of CD69 expression (right) shown in comparison to naïve in vivo (N; gray). **P = 0.0024, ***P < 0.0001 determined by two-way analysis of variance (ANOVA) with post hoc Tukey test. **c**, Representative dot plots of TCR_{TAG} IFN-γ and TNF production after 4 h ex vivo

TAG peptide stimulation, with inset numbers indicating the percentage of cells in each gate. Gates were set based on no peptide stimulation controls. **d**, Summary plots of the percentage of TNF/IFN-γ⁺ TCR_{TAG} after peptide stimulation and ex vivo GZMB expression. Each symbol represents an individual mouse. **e**, Histograms and summary plots of TOX expression. CD8⁺ Thy1.1 PD-1^{hi} endogenous (endo) dysfunctional T cells are shown as the positive control for TOX staining. Histograms show representative data for each group. NS, not significant. **P = 0.0036, ***P < 0.0001 determined by two-way ANOVA with post hoc Tukey test. Two independent experiments were carried out with 3–4 mice per group.

tumors but can occur in other advanced cancers in different tissues and with different tumor types and antigen specificities.

Dysfunction-associated epigenetic programs arise before division

Our finding of pre-division dysfunction in TST led us to ask whether dysfunction-associated epigenetic remodeling also occurred before cell division. We transferred CFSE-labeled TCR_{TAG} into tumor-bearing ASTxAlb-Cre or LM_{TAG}-infected B6 mice, sorted pre-division T-TCR_{TAG} (from liver tumors at 6 h, 12 h and 24 h) and E-TCR_{TAG} (from spleen at 6 h, 12 h and 24 h), and assessed chromatin accessibility by the assay for transposase-accessible chromatin with sequencing (ATAC-seq)²¹ and gene expression by RNA sequencing (RNA-seq; Fig. 5a and Extended Data Fig. 5a). Principle component analysis (PCA) of ATAC-seq and RNA-seq data showed that within 6 h, T-TCR_{TAG} and E-TCR_{TAG} had distinct chromatin accessibility and gene expression profiles (Fig. 5b and Extended Data Fig. 5b). Strikingly, the largest number of chromatin remodeling changes occurred during the first 6 h after activation, with fewer changes occurring at 12 h and 24 h (Fig. 5b,c). 64% of

differentially accessible chromatin peaks (DACs) were shared between E-TCR_{TAG} and T-TCR_{TAG} (Fig. 5d) and included TCR signaling downstream genes (*Irf4*, *Nfatc2*, *NfkB1*, *Lat*). Notably, a large number of peaks were more differentially accessible in T-TCR_{TAG} as compared to E-TCR_{TAG} (21%; Fig. 5d). *Pdcld* contains an enhancer peak 23 kb upstream from the transcription start site (~23-kb) previously shown to be preferentially opened in later dysfunctional/exhausted T cells in tumors⁵ and during chronic viral infection^{22–24}. Remarkably, we found that the ~23-kb ‘exhaustion’-associated *Pdcld* peak was more accessible within 6 h of T cell activation in tumors (Extended Data Fig. 5c). To identify potential TFs driving early chromatin remodeling differences, we used Chrom-Var²⁵ to perform motif analysis on DACs between E6-24h and T6-24 h. Motifs associated with inflammatory cytokine-induced TFs such as STAT family members were preferentially enriched in early E-TCR_{TAG} DACs (Fig. 5e), consistent with *Listeria*-induced innate immune activation^{26,27}. When we examined expression by RNA-seq, there were more differentially expressed genes (DEGs) with peaks containing STAT1 motifs in E-TCR_{TAG} compared to T-TCR_{TAG}, and gene expression changes mainly correlated with the direction of the peak change (Extended Data

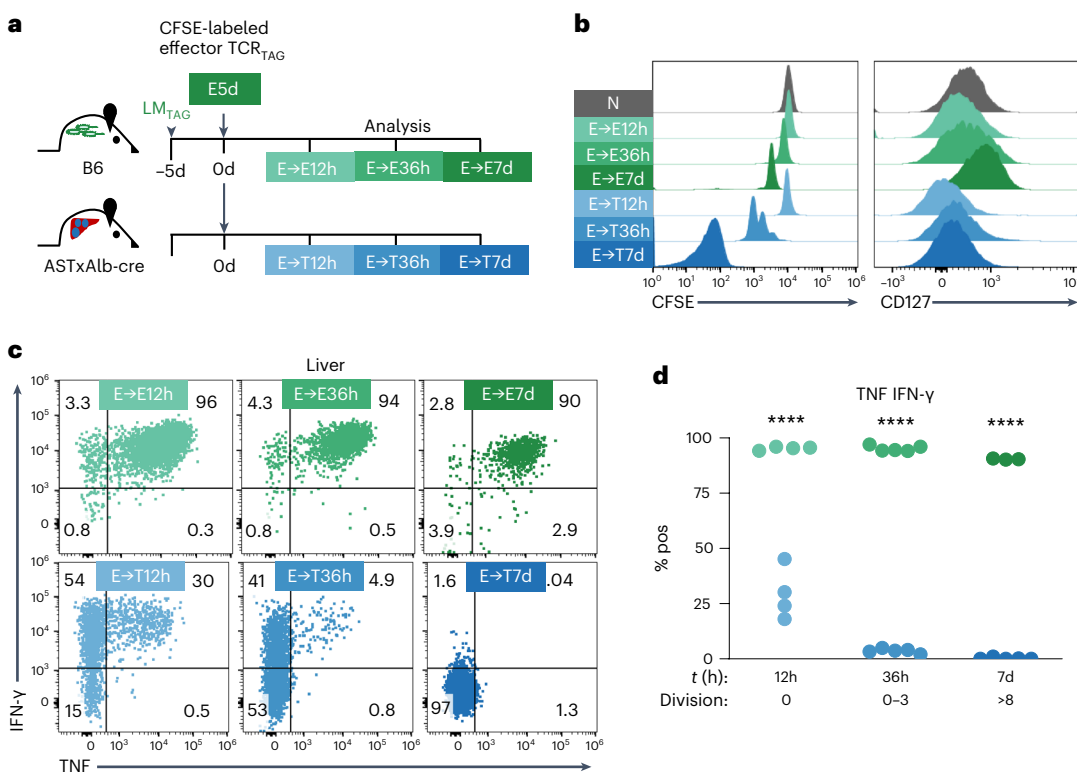


Fig. 3 | Committed effector CD8⁺ T cells rapidly lose function in tumor-bearing hosts. **a**, Experimental scheme: committed effectors were generated by transferring naive TCR_{TAG} into LM_{TAG}-infected B6 mice and collecting splenocytes 5 d after transfer (E5d). E5d were CFSE labeled and transferred into time-matched infected mice or tumor-bearing mice. TCR_{TAG} were re-isolated from infected (green) or tumor-bearing (blue) secondary recipients 12 h, 36 h and 7 d after transfer. All flow plots were gated on live CD8⁺Thy1.1⁺ cells. **b**, Representative histograms of CFSE dilution and CD127 expression from

spleens of infected animals and livers of tumor-bearing mice with naive TCR_{TAG} (N; gray) shown for comparison. **c**, Representative dot plots of TCR_{TAG} IFN- γ and TNF production after 4 h ex vivo TAG peptide stimulation from livers of infected mice or liver tumor-bearing mice, with inset numbers indicating the percentage of cells in each gate. Gates were set based on no peptide stimulation controls. **d**, Summary plots of the percentage of TNF⁺IFN- γ ⁺TCR_{TAG}. Each symbol represents an individual mouse with $n = 3-5$ per group pooled from two experiments.

**** $P < 0.0001$ determined by two-way ANOVA with post hoc Tukey test.

Fig. 6a). Upregulated genes containing STAT1 motif peaks encoded cytokine receptors, such as *Il12rb*, and inflammation-associated genes such as *Oasl1* (ref. 28). On the other hand, in TST, NFAT TF family motifs were enriched in DACs (Fig. 5e). We previously showed that NFAT drives expression of multiple inhibitory receptors⁵ as well as the TF TOX¹⁷ in TST at later time points. Thus, alterations in NFAT activity in TST begin within hours of activation and may result from NFAT association with different TF partners or genomic locations²⁹ as compared to T cells in acute infection.

Gene-set enrichment analysis (GSEA) showed that early activated TCR_{TAG} in infected mice and tumor-bearing mice as compared to naive TCR_{TAG} shared enrichment for genes associated with T cell activation (Extended Data Fig. 6b). T-TCR_{TAG} and E-TCR_{TAG} also shared enrichment for gene sets associated with purine/pyrimidine metabolism, MYC targets, translation, glycolysis and oxidative phosphorylation, known to be induced following TCR activation³⁰ (Extended Data Fig. 6b). When we compared T-TCR_{TAG} and E-TCR_{TAG} head-to-head, we found that early E-TCR_{TAG} were enriched for gene sets associated with IFN- α and IFN- γ responses (Fig. 5f), consistent with STAT TF motif enrichment in DACs (Fig. 5e). In contrast, early T-TCR_{TAG} were enriched for gene sets expressed in T cells stimulated in the absence of signal 3/inflammation (Fig. 5f). These analyses suggest that T cells activated in infected and tumor-bearing hosts received similar TCR stimulation; however, T cells activated in tumor-bearing hosts failed to receive inflammatory cytokine signaling present in infected hosts.

We next asked how pre-division infection and tumor-activated TCR_{TAG} transcriptional profiles compared with T cell profiles at later

time points. Early E-TCR_{TAG} showed enrichment for gene sets associated with later effector (day 6) and memory T cells (day 30) from acute infection (Fig. 5f). In contrast, early T-TCR_{TAG} showed enrichment for gene sets associated with later dysfunctional/exhausted T cells in tumors (day 5–30) or chronic viral infection (day 30; Fig. 5f). In line with these findings, T-TCR_{TAG} induced greater expression of negative regulators of T cell function (*Rgs16*, *Pdcd1*, *Ptpn22*) and lower expression of inflammation-associated genes (*Mx1*, *Isg15*), genes encoding cytokines/cytolytic mediators (*Jfng*, *Gzmb*, *Gzma*) and genes encoding TFs associated with functional differentiation (*Batf*, *Tbx21*)³¹ (Fig. 5g). T-TCR_{TAG} expressed more *Bach2* and *Id3*, previously associated with memory phenotypes³² and restraint of effector differentiation (Fig. 5g)³³. Taken together, our data demonstrate that epigenetic and transcriptional changes previously associated with late-stage dysfunctional/exhausted T cells are already induced within hours of activation in tumor-bearing hosts.

Chromatin remodeling is reinforced with time/tumor antigen

We next asked whether pre-division dysfunction-associated chromatin accessibility changes are maintained or evolve with time and continued antigen exposure. We compared chromatin accessibility in T6h-T24h with our previously published chromatin accessibility data in TCR_{TAG} isolated from liver tumors after 5–60 d⁵. We also carried out ATAC-seq on TCR_{TAG} sorted from ASTxAlb-Cre after 5 d (T5d) and 10 d (T10d). PCA showed that TST chromatin accessibility clustered into three groups based on the duration of tumor exposure: early (6–24 h), intermediate (5–10 d) and late (14–60+ d; Fig. 6a). T5d from malignant liver lesions

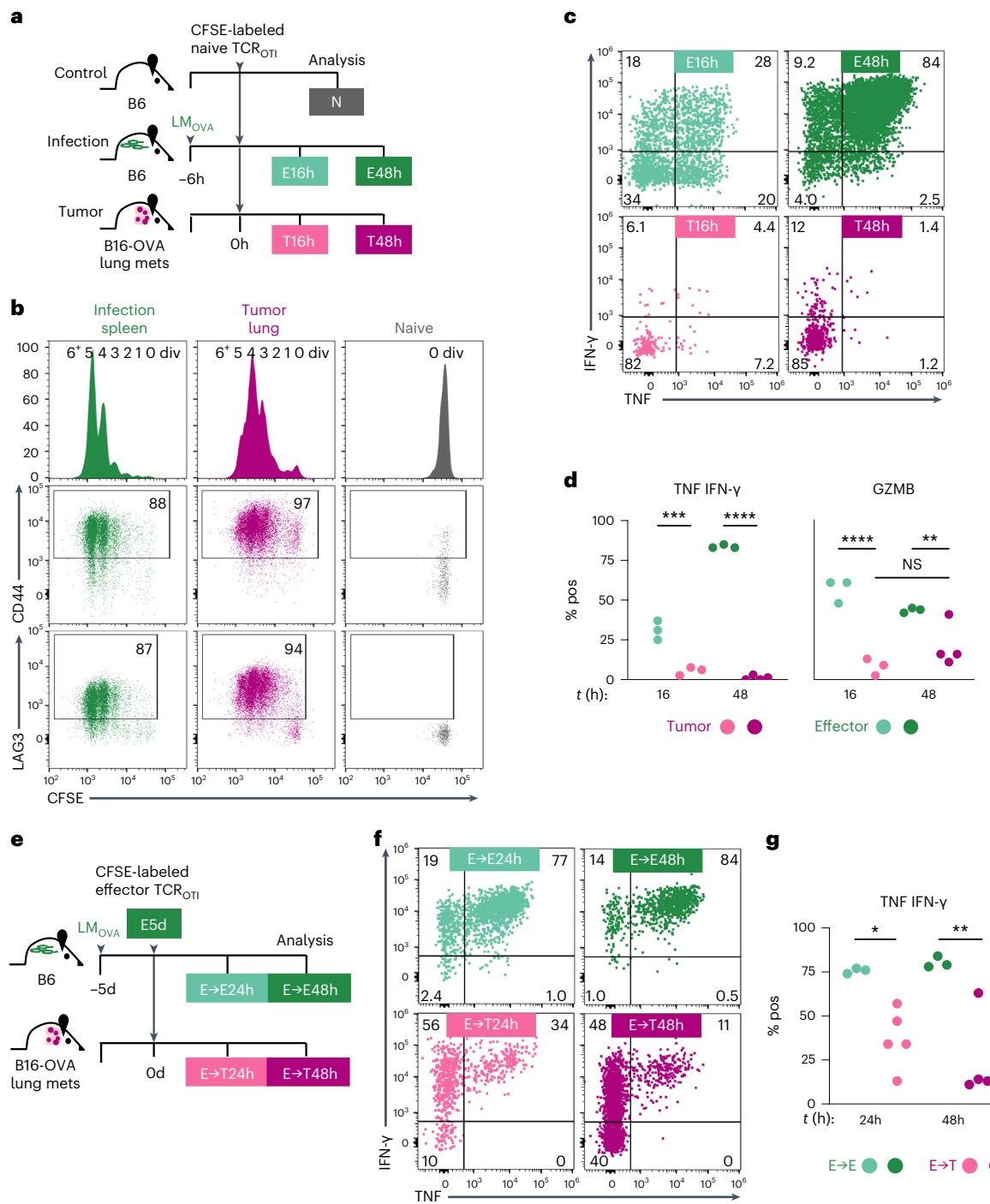
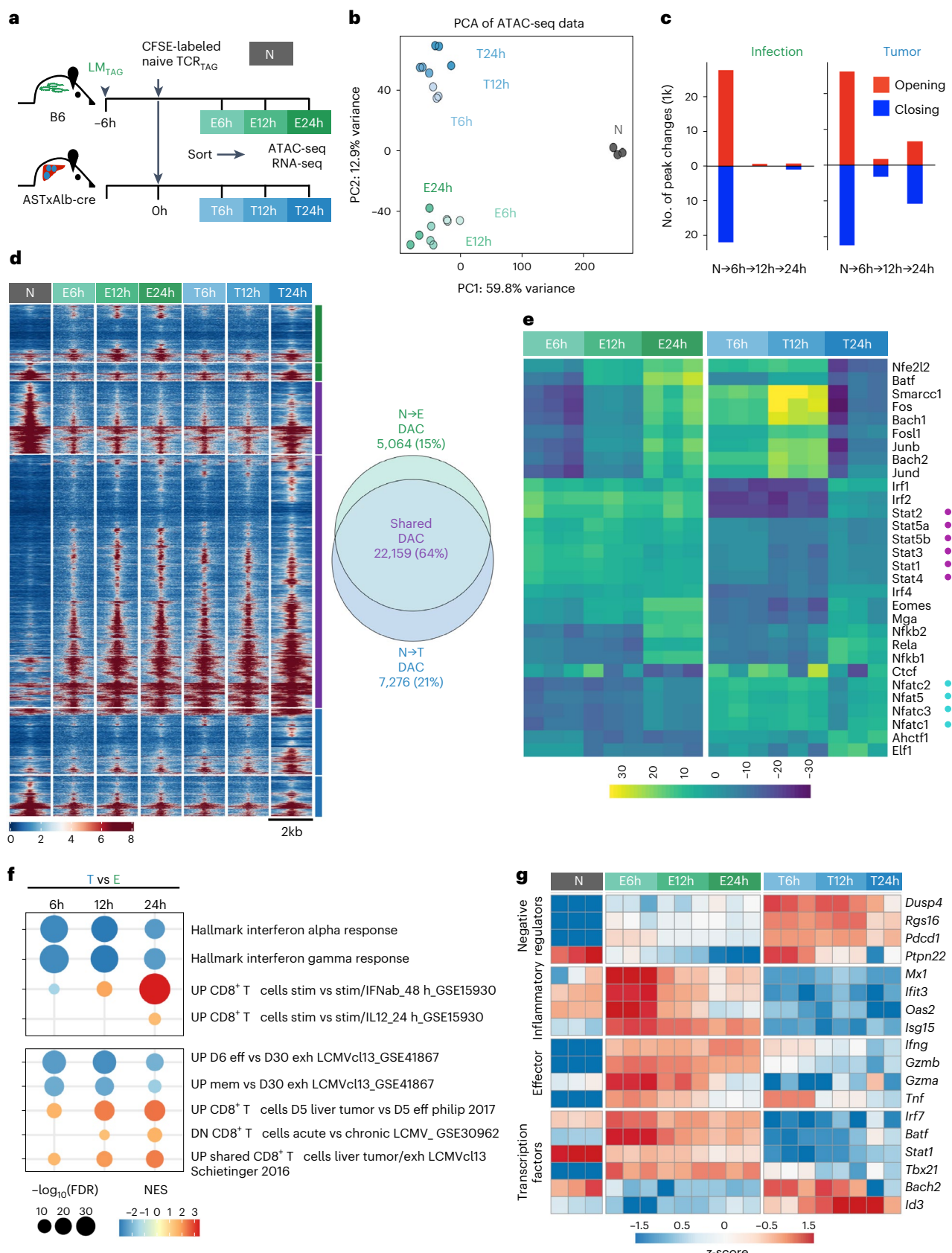


Fig. 4 | Naive and effector tumor-specific T cells robustly proliferate in mice with metastatic melanoma but lack effector function. **a**, Experimental scheme: CFSE-labeled naïve TCR_{OTI} (Ly5.1) were adoptively transferred into B6 (Ly5.2), LM_{OVA}-infected B6 (Ly5.2) or B6 (Ly5.2) with pulmonary B16-OVA metastases, and lymphocytes were re-isolated from infected spleens (green) or tumor lungs (pink) at 16 h and 48 h after transfer for analysis by flow cytometry. **b**, TCR_{OTI} CFSE dilution (upper) with CD44 and LAG3 versus CFSE dilution (lower) at 48 h shown in comparison to N, with inset numbers indicating the percentage of cells in each gate. Gates were set based on N. Each plot shows data concatenated from 3–4 mice per group. **c**, TCR_{OTI} IFN- γ and TNF production after 4 h ex vivo OVA peptide stimulation, with inset numbers indicating the percentage of cells in each gate. Gates were set based on no peptide stimulation controls. **d**, Summary plots of the percentage of TNF $^+$ IFN- γ $^+$ TCR_{OTI} after 4 h ex vivo OVA peptide stimulation and ex vivo GZMB expression. Each symbol

represents an individual mouse. Two independent experiments were carried out with 3–4 mice per group. ** P = 0.0012, *** P = 0.0005 and **** P < 0.0001 determined by two-way ANOVA with post hoc Tukey test. **e**, Experimental scheme: committed effectors were generated by transferring naïve TCR_{OTI} into LM_{OVA}-infected B6 mice and collecting splenocytes 5 d after transfer (E5d). E5d were CFSE labeled and transferred into time-matched LM_{OVA}-infected B6 or B6 with pulmonary B16-OVA metastases. TCR_{OTI} were re-isolated from infected spleens (green) or lung tumors (pink) of secondary recipients 24 h and 48 h after transfer. All flow plots were gated on live CD8 $^+$ Ly5.1 $^+$ cells. **f**, TCR_{OTI} IFN- γ and TNF production after 4 h ex vivo OVA peptide stimulation, with inset numbers indicating the percentage of cells in each gate. Gates were set based on no peptide stimulation controls. **g**, Summary plots of the percentage of TNF $^+$ IFN- γ $^+$ TCR_{OTI}, where each symbol represents an individual mouse. * P = 0.017 and ** P = 0.0023 determined by two-way ANOVA with post hoc Tukey test.



(ASTxAlb-Cre; 2023) had similar chromatin accessibility profiles as T5d isolated from premalignant liver lesions (ASTxCre^{ERT2}; 2017; Fig. 6a). The greatest number of TST DAC changes occurred within 6 h, with another large round of changes between 24 h and 5 d, and a

third smaller round between 7 d and 14 d, after which there was little chromatin remodeling (Fig. 6b and Extended Data Fig. 7a). TCR_{TAG} in the setting of acute infection also had many early peak changes within 6 h and a second round of peak changes between 24 h and 5 d; however,

Fig. 5 | Dysfunction-associated epigenetic programming begins before cell division. **a**, Experimental scheme: CFSE-labeled naive TCR_{TAG} (Thy1.1) were adoptively transferred into LM_{TAG}-infected B6 (Thy1.2), or ASTxAlb-Cre (Thy1.2) mice, and TCR_{TAG} were flow-sorted from spleens and livers at 6 h, 12 h and 24 h after transfer (Extended Data Fig. 5a). **b**, PCA comparing chromatin accessibility in naive (N; gray) and TCR_{TAG} differentiating during acute infection (green) and in tumors (blue) at 6 h, 12 h and 24 h after transfer by the top 25×10^3 variable peaks. Each symbol represents a single biological replicate. **c**, Number of DACs during each transition (opening peaks, red; closing peaks, blue; false discovery rate (FDR) < 0.05). **d**, Chromatin accessibility heat map. Each row represents one of 34,449 peaks (FDR < 0.05, $|\log_2\text{FC}| > 1.5$) displayed over a 2-kb window centered on the peak summit. Scale units are reads per genomic content (RPGC) normalized to 1x sequencing depth for 20-bp bins with blue indicating

closed chromatin and red indicating open chromatin. Peaks are ordered by membership within each subset shown in the Venn diagram (right) and hierarchical clustering within the subset. Venn diagram showing DACs in TCR_{TAG} at early time points in infection, tumors or shared in infection and tumors. **e**, Heat map of chromVAR computed deviations z-score for the top 30 most variable TF motifs enriched in DACs from TCR_{TAG} from tumors and infected mice at 6 h, 12 h and 24 h. Purple dots denote STAT TF family motifs enriched in effectors and blue dots denote NFAT TF family motifs enriched in TST. **f**, GSEA on TCR_{TAG} from tumors (T) relative to infection (E) at 6 h, 12 h and 24 h. Color represents normalized enrichment score (NES) and circle size represents the negative $\log_{10}(\text{FDR})$. **g**, Heat map showing selected differential gene expression between naive TCR_{TAG} and TCR_{TAG} in tumors or infection at 6 h, 12 h and 24 h (FDR < 0.05, $|\log_2\text{FC}| > 1$), z-score normalization across rows.

in contrast to TST in tumors that underwent a third wave of chromatin remodeling, likely driven by continued tumor antigen exposure, few peak changes occurred after E5d (Fig. 6b and Extended Data Fig. 7a,b), demonstrating that the memory-associated chromatin state was largely established early by day 5 upon pathogen/antigen clearance.

We next compared how individual DACs changed over time by plotting the fold change of each peak's accessibility during the early transition (naive (N) to 6 h) versus during the intermediate (int) transition (24 h to 5 d; Fig. 6c,d). Thus, a peak in the 'reinforced open' quadrant in the scheme in Fig. 6c had an increase in accessibility between N and 6 h with a further increase in accessibility between 24 h and 5 d. In contrast, a peak in the 'stable closed' quadrant had an early decrease in accessibility and remained 'closed' during the later transition. This analysis revealed that 36% of pre-division remodeled chromatin peaks in TST remained stable (19% closed, 17% open) with continued tumor/antigen exposure, with additional peaks reinforced with time (13%) or opening at the intermediate transition (int, 16%; Fig. 6d). Thus, nearly 50% (stable + reinforced) of the T5d chromatin accessibility signature was already established within the first 6 h after activation in tumors. This was in marked contrast with differentiation during infection, in which many early DACs were transient (51%) or newly occurring between 24 h and 5 d (int 19%; Fig. 6d). While tumor-activated and infection-activated T cells underwent some chromatin remodeling during the intermediate-to-late (T14d or M) transition, most chromatin accessibility changes (> 60%) remained stable (Extended Data Fig. 7c). The *Pdcd1* locus exemplifies these patterns, with peak changes maintained and reinforced with time in tumors and transient during acute infection-induced effector/memory differentiation (Fig. 6e,f), consistent with PD-1 surface expression (Extended Data Fig. 1a). The dysfunction/exhausted-associated -23-kb *Pdcd1* enhancer peak opened early only in tumors and was reinforced at later time points, while the peak at +4.5 kb, transiently opened during infection, remained stably opened in tumors, and the peak at +10 kb opened only at the intermediate time point (int open) in tumors (Fig. 6e).

To identify potential TFs driving specific transitional peak changes during effector and TST differentiation, we carried out MOTif aNALysis with Lisa (monaLisa)³⁴. While TF enrichment in the transiently opened peaks (light purple) was overall similar between E-TCR_{TAG} and T-TCR_{TAG}, NFAT TF family motifs were particularly enriched in peaks with reinforced (light orange) and later/intermediate (dark orange) opening in tumors but not during infection (Fig. 6g), consistent with TCR_{TAG} receiving continuous antigen/TCR stimulation in tumors but only transient stimulation during acute infection. In contrast, T-box TF family motifs, including those of TBET (TBX21) and EOMES, were more enriched in peaks that opened early and were predominantly reinforced (light orange) during infection, but less so in tumors (Fig. 6g), consistent with the role of these TFs in facilitating functional effector formation during acute infection and functional memory populations following pathogen/antigen clearance^{35–38}.

Tumor exposure duration determines dysfunction imprinting

Given the observation that many chromatin accessibility changes in TCR_{TAG} were stabilized and/or reinforced with increased tumor/antigen exposure, we next asked if TCR_{TAG} removed from tumors and transferred to tumor-free hosts would retain the functional, immunophenotypic and epigenetic hallmarks of dysfunction. TCR_{TAG} were re-isolated from liver tumors after 1, 5 or 10 d (T24h, T5d and T10d) and parked in tumor-free B6 mice (P24h, P5d and P10d) for 5 d (Fig. 7a). In parallel with functional and immunophenotypic analysis, we carried out ATAC-seq on the pre-parking and post-parking samples. Before transfer, tumor-activated TCR_{TAG} failed to make cytokines (Fig. 7b). After 5 d of parking, P24h had uniformly downregulated PD-1 (Fig. 7c), yet 35–40% remained unable to produce TNF or IFN-γ (Fig. 7b,d). With longer tumor exposure, more TCR_{TAG} had 'imprinted' effector function loss, with nearly all P10d failing to make effector cytokine and retaining PD-1 expression (Fig. 7b,c).

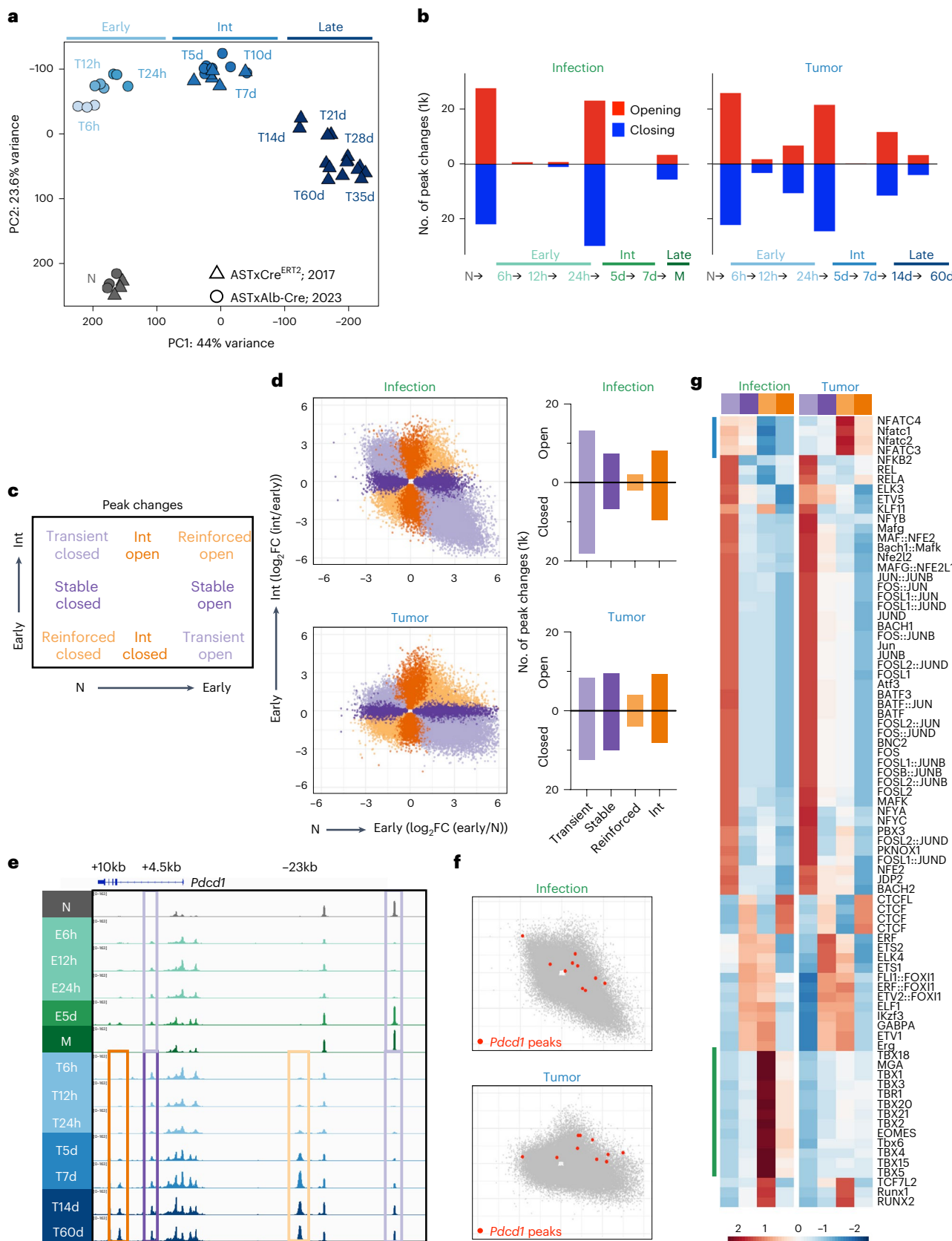
Heterogeneity has been described for dysfunctional/exhausted T cells, with more stem-like TCF1⁺ dysfunctional/exhausted T cells

Fig. 6 | Pre-division tumor-induced tumor-specific T cell chromatin remodeling is reinforced with time and tumor antigen exposure. **a**, PCA comparing chromatin accessibility in naive TCR_{TAG} (N) and TST after 6 h, 12 h and 24 h (early), 5 d, 7 d and 10 d (intermediate; int), 14 d, 21 d, 28 d, 35 d and 60 d+ (late). Circles indicate TCR_{TAG} in liver tumor-bearing ASTxAlb-Cre from the current study (2023) and triangles: TCR_{TAG} in premalignant and malignant liver tumor-bearing ASTxAST-Cre^{ERT2}, previously published (2017)⁵. **b**, Number of peak changes during CD8⁺ T cell differentiation in infection (left) and tumors (right) across (opening peaks, red; closing peaks, blue) FDR < 0.05. **c**, Legend for **d–g** identifying scatterplot quadrants of peak changes during early (x axis) versus later (y axis) transitions. **d**, Upper, peak changes during naive (N) → early (E6h) transition ($\log_2\text{FC}$ E6h/N) versus early → int (E5 d) transition ($\log_2\text{FC}$ E5 d/E24 h). Lower, peak changes during N → early (T6h) transition ($\log_2\text{FC}$ T6h/N) versus early → int (T5 d) transition ($\log_2\text{FC}$ T5 d/T24 h). Each point represents an individual peak colored as in **c**. To the right, bar plots show the number of

peaks in each quadrant (opening peaks above axis and closing peaks below axis; FDR < 0.05 for either comparison). **e**, TCR_{TAG} *Pdcd1* locus accessibility profile across time points during infection and in liver tumors. Boxes highlighting peaks are colored as in **c**. The exhaustion-associated -23-kb peak in *Pdcd1* is highlighted in light orange denoting an opening peak reinforced during tumor progression. Light purple boxes highlight transiently closed and open peaks. For T-TCR_{TAG}, the dark purple box highlights an opened peak maintained at later time points, and the dark orange box highlights a peak that opened at the later time points. **f**, Scatterplot highlighting individual *Pdcd1* peaks (red) relative to overall peaks (gray). **g**, MOTif aNALysis with Lisa (monaLisa) showing enriched TF motifs for each set of peaks classified as in **c** and **d** during the early (N → 6 h) and intermediate (24 h → 5 d) transitions in infection and tumor. Highlighted are NFAT TF family members, enriched in tumor reinforced and intermediate opening peaks, and T-box TF family members, enriched in infection reinforced and intermediate opening peaks.

needed to sustain antiviral/antitumor effects^{39–42} and reviewed in ref. 16. To determine whether such heterogeneity explained the partial recovery of effector function observed in P24h and P5d, we examined TCR_{TAG} expression of stem/progenitor versus terminal differentiation

markers at early, intermediate and late time points (Extended Data Fig. 8a). At 36 h after transfer into ASTxAlb-Cre mice, undivided and early division TCR_{TAG} in the livers and spleens of ASTxAlb-Cre mice uniformly expressed TCF1 at the same or higher level as naive TCR_{TAG}



(Extended Data Fig. 8b). In contrast, T60+d in the liver had markedly downregulated TCF1 (Extended Data Fig. 8b). To look for evidence of bimodal stem/progenitor versus terminally differentiated populations, we examined concurrent expression of CD38 and CD101, surface markers correlated with a terminally differentiated dysfunctional state and loss of reprogrammability⁵. T36h and T5d remained low for both CD38 and CD101, in contrast to T60+d, which were CD38⁺ and heterogeneous for CD101 (Extended Data Fig. 8c). T36h and T5d also showed homogeneous expression of TCF1 and TOX, becoming TCF1^{lo} and TOX^{hi} only at later time points (T60+d; Extended Data Fig. 8c). Thus, the dichotomous marker expression previously associated with stem/progenitor and terminally differentiated exhausted T cells does not clearly correlate with the ability of early TST to recover cytokine function after parking. We cannot exclude the possibility that smaller, more graded expression changes at the individual-cell level may regulate or predict cytokine recovery.

When we assessed chromatin accessibility, we found that the post-parking samples clustered separately from pre-parking samples or from antigen-experienced memory T cells (Fig. 7e,f). We used a similar scatterplot analysis as described in Fig. 6c to characterize pre-parking and post-parking peak changes (DACs). Many peak changes in T24h were transient, reverting after 5 d of parking in tumor-free hosts, and there were fewer stable peaks (Fig. 7g). However, with longer tumor exposure, the number of transient peaks decreased while the number of stable peaks increased (Fig. 7g). Correspondingly, chromatin accessibility at the *Pdcld* –23-kb enhancer in post-parking TCR_{TAG} increased with longer tumor exposure (Extended Data Fig. 9a). In contrast, TOX expression was uniformly lost after TCR_{TAG} removal from tumors, even after 10 d of tumor exposure, (Fig. 7c,d), suggesting that TOX expression is dependent on continued antigen/TCR stimulation and/or requires even longer tumor exposure to become imprinted. Recent studies showed that later exhausted T cells (>30 d exposure) from humans and murine models of chronic viral infection retain TOX expression together with exhaustion-associated chromatin peaks ('epigenetic scarring') after transfer to antigen-free hosts or viral cure with direct-acting antiviral therapy^{43–45}. While we observed evidence of 'epigenetic scarring' in some *Tox* locus peaks, other peaks, particularly peaks that appeared during the intermediate and late time points, were not retained in post-parking TCR_{TAG} (Extended Data Fig. 9b).

To identify the drivers of progressive imprinting of dysfunction hallmarks, we asked how TF motif enrichment changed in pre-parking and post-parking DACs. Open chromatin peaks in post-parking TCR_{TAG} showed enrichment for CTCF motifs (Fig. 7h), intriguing in light of recent studies showing that CTCF-mediated genome reorganization promotes CD8⁺ T cell effector differentiation⁴⁶. NFAT TF family enrichment, which increased in intermediate TCR_{TAG}, was lost upon removal from tumors (Fig. 7h), suggesting that NFAT-mediated DACs are maintained by continued TCR signaling. Post-parking samples clustered closer to memory TCR_{TAG} than did pre-parking samples (Fig. 7e,f).

possibly reflecting the fact that post-parking and memory TCR_{TAG} are not undergoing antigen/TCR stimulation. However, memory TCR_{TAG} produce high levels of TNF and IFN-γ upon antigen restimulation (Fig. 3 and refs. 5,15), whereas the post-parking TCR_{TAG} largely failed to do so (Fig. 7b). We used HOMER⁴⁷ to compare TF motif enrichment in chromatin peaks in P5d and M and found that KLF family motifs were predominant in nonfunctional post-parking TCR_{TAG} peaks (Fig. 7i), consistent with previously described roles in T cell quiescence, functional restraint and fixed dysfunction^{5,48,49}. In contrast, memory TCR_{TAG} showed enrichment for memory-associated TCF1 and ZEB family^{50–52} family motifs, lacking in P5d (Fig. 7i). Interestingly, the *Ifng* locus contained a peak uniquely accessible in memory TCR_{TAG} (+14 kb) that was not present in pre-parking and post-parking tumor samples (Extended Data Fig. 9c). This peak was previously shown to be accessible in functional NK cells and to bind TBET⁵³. In contrast, a peak in *Ifng* at +19 kb was not present in memory TCR_{TAG} but present in both pre-parking and post-parking TSTs. Thus, removing T cells from tumors at early and intermediate time points may reverse TCR-driven inhibitory signals and some dysfunction-associated chromatin remodeling; however, effector function is not recovered because T cells activated in tumors have failed to induce function/memory-defining TFs.

Discussion

Here, we describe the functional, immunophenotypic, epigenetic and transcriptional features of TST differentiation within the hours following tumor antigen encounter in vivo. Although TST were activated and proliferated similarly to CD8⁺ T cells during acute infection, TST in tumor-bearing hosts failed to gain both effector cytokine and cytolytic function. Remarkably, this dysfunction was evident even before cell division. Rapid effector function impairment in vivo coincided with extensive chromatin remodeling and transcriptional alterations in TST within 6 h after tumor antigen encounter, including hallmark chromatin accessibility changes previously characterized as 'exhaustion associated.' These findings upend the paradigm that tumor-induced T cell dysfunction requires chronic antigen stimulation over days to weeks and instead show that CD8⁺ T cells integrate multiple signaling inputs (TCR, co-stimulatory/inhibitory and cytokine) immediately following activation in different contexts, which dictate their epigenetically encoded differentiation to the functional effector state (infection) or to the dysfunctional state (tumors).

Proliferation and differentiation are intimately connected throughout development⁶, and previous studies show that proliferation is required for the epigenetic remodeling associated with differentiation for thymocytes and other adaptive immune lineages^{7–10}. However, we find that CD8⁺ T cells execute large-scale chromatin remodeling and differentiation before undergoing cell division and it remains to be seen whether other immune cells similarly undergo early rapid differentiation to the functional or dysfunctional state. Nevertheless, despite losing effector function, dysfunctional TST

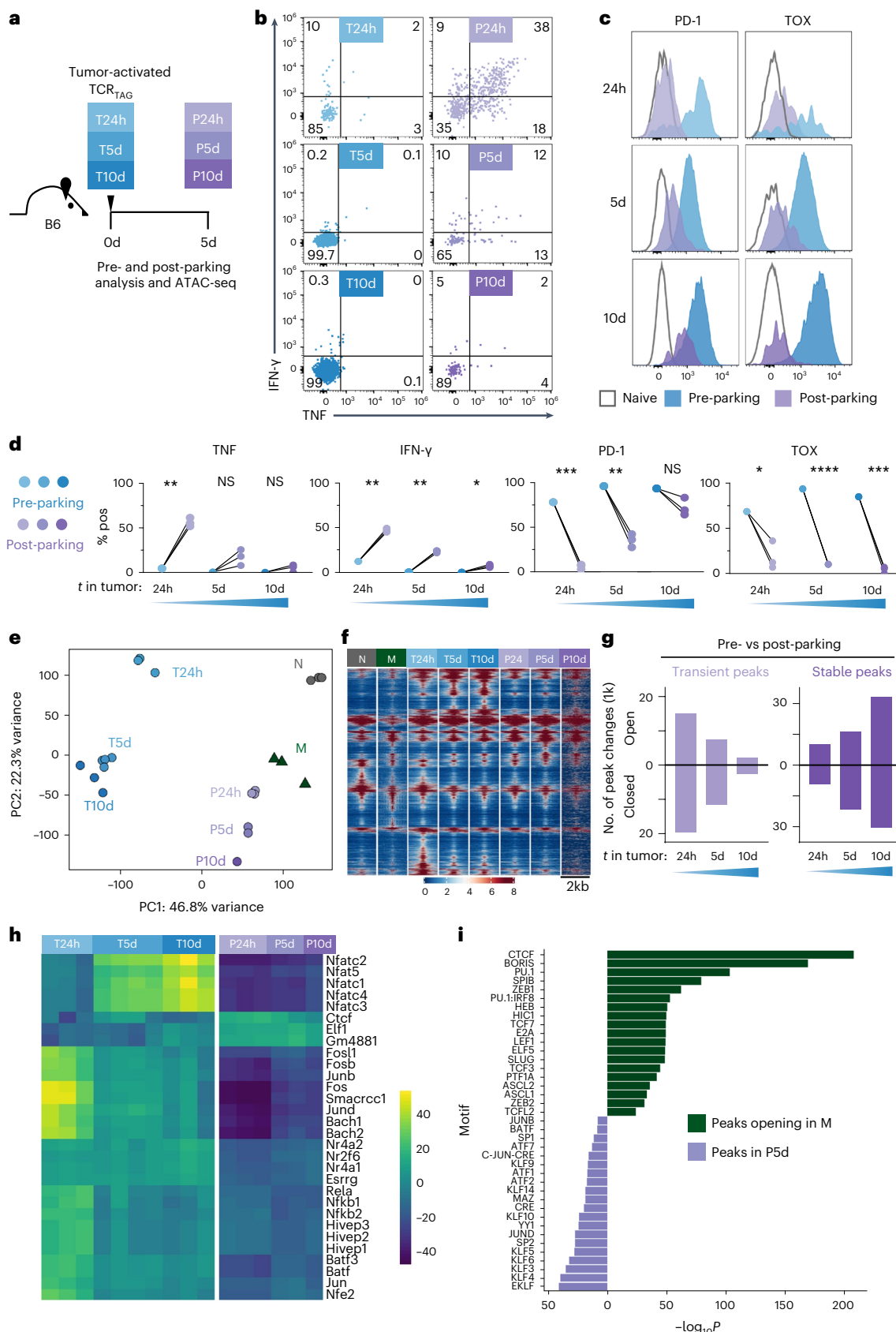
Fig. 7 | Duration of tumor antigen exposure determines dysfunction stability and imprinting. **a**, Experimental scheme: TCR_{TAG} adoptively transferred into ASTxAlb-Cre for 24 h, 5 d or 10 d (pre-parking) were isolated from tumors, transferred into tumor-free B6 mice, parked for 5 d (post-parking), and then isolated from secondary hosts (P24 h, P5 d and P10 d) and analyzed. **b**, Live CD8⁺ Thy1.1⁺ TCR_{TAG} analyzed pre-parking (left) and post-parking (right). IFN-γ and TNF production after 4 h ex vivo TAG peptide stimulation, with inset numbers indicating the percentage of cells in each gate. Gates were set based on no peptide stimulation controls. **c**, Histogram plots of pre-parking TCR_{TAG} (blue) and concatenated post-parking samples (purple), with naive (N; open gray) for comparison. TCR_{TAG} were exposed to tumors for 24 h (upper), 5 d (middle) and 10 d (lower) before transfer to tumor-free hosts. **d**, Summary plots show the percentage TNF⁺, IFN-γ⁺, PD-1⁺ and TOX⁺ pre-parking (for pooled donor TCR_{TAG} from 3–4 mice) and post-parking (each symbol represents an individual mouse). TNF, **P = 0.003. IFN-γ, **P = 0.0013, 0.0011 and *P = 0.0191. PD-1, ***P = 0.0005,

P = 0.0049. TOX, *P = 0.037, **P < 0.0001 and ***P = 0.0007. Statistical significance determined for change from baseline by one-sample Student's t-test. Two independent experiments were carried out with n = 2–4 mice per group. **e**, PCA comparing chromatin accessibility in naive (N; gray), memory, (M; green), TCR_{TAG} pre-parking (T24h, T5d and T10d; blue) and post-parking (P24h, P5d and P10 d; purple) by the top 25 × 10³ variable peaks. Each symbol represents an individual biological replicate. **f**, Chromatin accessibility heat map in naive (N), memory (M) and pre-parking and post-parking TCR_{TAG}. Each row represents one of 58,834 peaks (differentially accessible between at least one comparison; FDR < 0.05, |log₂FC| > 1.5) displayed over a 2-kb window centered on the peak summit. **g**, Number of chromatin peaks that are transient or stable post-parking (determined as in Fig. 5c) relative to pre-parking. **h**, Heat map of chromVAR computed deviations z-score for the top 30 most variable TF motifs across TCR_{TAG} pre-parking and post-parking. **i**, Paired comparison of enriched TF motifs by HOMER between M and post-parking P5 d TCR_{TAG}.

proliferated rapidly and robustly; thus, the regulation of proliferation and functional effector differentiation is uncoupled. This finding, in line with previous studies in vitro or in self-tolerance models^{54–56} has important implications for cancer immunotherapy, as efforts aimed

at boosting TST proliferation by gene targeting may not be sufficient to reverse effector function loss.

While dysfunctional hallmarks, including impaired effector function, inhibitory receptor expression and dysfunction/exhaustion-associated



chromatin accessibility changes, were manifested in TST with different kinetics before cell division, with continued tumor/antigen stimulation and proliferation, TST underwent additional chromatin remodeling that stabilized and reinforced initial dysfunction epigenetic programs. These findings together with our previous work^{5,17} demonstrate that the T cell dysfunctional state is composed of different modules (loss of effector function, upregulation of inhibitory receptors, proliferative capacity), which are regulated independently. This was borne out when we tested the degree to which early TST dysfunction was ‘imprinted’—that is, retained upon removal from the tumor and transfer into tumor-free hosts. Effector function impairment was not reversed upon tumor removal in a significant fraction of TST exposed to tumors for 24 h, in contrast to PD-1 expression, which was nearly absent in P24h and did not become fixed until after 5+ d of tumor exposure, with epigenetic reinforcement.

The heterogeneity in effector function recovery observed upon early TST removal to tumor-free hosts raised the question as to whether there was bifurcation in early/intermediate time point populations toward stem/progenitor or terminally differentiated dysfunctional/exhausted states. However, in contrast to studies in chronic LCMV infection models⁵, we found that early/intermediate TST had homogeneous expression of TCF1 and did not express late/terminal exhaustion/dysfunction markers. While TST dysfunction shares many features with the chronic viral infection-induced exhaustion, there are important biological differences between hosts with late-stage tumors and hosts with chronic infection that may be particularly relevant during the initial hours and days immediately following activation. Early time point TST did not show induction of inflammation-associated TFs or downstream inflammation-associated genes, and this lack of innate/inflammatory cytokine stimulation may lead to the failure of TST to induce functional/memory-associated gene programs, even upon removal from tumors. In contrast, chronic viral infection does induce innate immune signaling, and indeed, CD8⁺ T cells activated during acute and chronic viral infection have comparable effector function, with loss of cytokine and cytolytic function occurring over days to weeks⁵⁸.

Taken together, our studies suggest that there are two major contributing factors to TST dysfunction in hosts with late-stage tumors. First, TST activated in tumors or secondary lymphoid organs may receive strong TCR signaling due to a surfeit of tumor antigen, leading to robust activation and proliferation; however, the lack of innate inflammatory signals in tumors leads to a failure to induce TF regulating functional effector differentiation. Second, persistent tumor antigen/TCR stimulation and/or other negative regulatory signals in tumor-bearing hosts leads to ongoing NFAT activity or partnerless NFAT activity, further impairing effector function and inducing TOX expression as well as multiple other negative regulators of T cell signaling and function. In addition, chronic tumor antigen/TCR stimulation reinforces epigenetic programs encoding dysfunctional hallmarks, eventually leading to fixed dysfunctional TST.

The rapid loss of function in committed effector CD8⁺ T cells upon transfer into mice with late-stage liver and pulmonary melanoma metastases was particularly striking, demonstrating that the negative regulatory factors in hosts with advanced tumors can overwrite functional epigenetic programs in CD8⁺ T cells. Thus, even T cells that have been optimally activated in tumor-bearing hosts (for example through immunization or by activated antigen-presenting cells in draining lymph nodes), may still succumb to tumor-induced dysfunction upon entry into tumors. These findings have important implications for immunotherapies such as adoptive T cell therapies and immune checkpoint blockade.

Given how rapidly CD8⁺ T cells acquire dysfunctional hallmarks in tumor-bearing hosts, with early epigenetic remodeling further reinforced over time/tumor progression, we need to target both early dysfunction induction as well as dysfunction reinforcement in order to improve T cell-based cancer immunotherapy. Further studies are

needed to understand how CD8⁺ T cells rapidly integrate TCR and context-dependent inputs to make fate choices. By deciphering the complex network of signaling and gene regulatory networks driven by TCR and context-dependent inputs, we can design better strategies to alter or redirect T cells into functional cancer killers.

Online content

Any methods, additional references, Nature Portfolio reporting summaries, source data, extended data, supplementary information, acknowledgements, peer review information; details of author contributions and competing interests; and statements of data and code availability are available at <https://doi.org/10.1038/s41590-023-01578-y>.

References

- Williams, M. A. & Bevan, M. J. Effector and memory CTL differentiation. *Annu. Rev. Immunol.* **25**, 171–192 (2007).
- McLane, L. M., Abdel-Hakeem, M. S. & Wherry, E. J. CD8 T cell exhaustion during chronic viral infection and cancer. *Annu. Rev. Immunol.* **37**, 457–495 (2019).
- Waugh, K. A. et al. Molecular profile of tumor-specific CD8⁺ T cell hypofunction in a transplantable murine cancer model. *J. Immunol.* **197**, 1477–1488 (2016).
- Mognol, G. P. et al. Exhaustion-associated regulatory regions in CD8⁺ tumor-infiltrating T cells. *Proc. Natl Acad. Sci. USA* **114**, E2776–E2785 (2017).
- Philip, M. et al. Chromatin states define tumour-specific T cell dysfunction and reprogramming. *Nature* **545**, 452–456 (2017).
- Zhu, L. & Skoultchi, A. I. Coordinating cell proliferation and differentiation. *Curr. Opin. Genet. Dev.* **11**, 91–97 (2001).
- Kreslavsky, T. et al. Beta-selection-induced proliferation is required for αβ T cell differentiation. *Immunity* **37**, 840–853 (2012).
- Bird, J. J. et al. Helper T cell differentiation is controlled by the cell cycle. *Immunity* **9**, 229–237 (1998).
- Tangye, S. G. & Hodgkin, P. D. Divide and conquer: the importance of cell division in regulating B-cell responses. *Immunology* **112**, 509–520 (2004).
- Scherer, C. D., Barwick, B. G., Guo, M., Bally, A. P. R. & Boss, J. M. Plasma cell differentiation is controlled by multiple cell division-coupled epigenetic programs. *Nat. Commun.* **9**, 1698 (2018).
- Kaech, S. M. & Ahmed, R. Memory CD8⁺ T cell differentiation: initial antigen encounter triggers a developmental program in naïve cells. *Nat. Immunol.* **2**, 415–422 (2001).
- van Stipdonk, M. J., Lemmens, E. E. & Schoenberger, S. P. Naïve CTLs require a single brief period of antigenic stimulation for clonal expansion and differentiation. *Nat. Immunol.* **2**, 423–429 (2001).
- Williams, M. A. & Bevan, M. J. Shortening the infectious period does not alter expansion of CD8 T cells but diminishes their capacity to differentiate into memory cells. *J. Immunol.* **173**, 6694–6702 (2004).
- Bevan, M. J. & Fink, P. J. The CD8 response on autopilot. *Nat. Immunol.* **2**, 381–382 (2001).
- Schietinger, A. et al. Tumor-specific T cell dysfunction is a dynamic antigen-driven differentiation program initiated early during tumorigenesis. *Immunity* **45**, 389–401 (2016).
- Philip, M. & Schietinger, A. CD8⁺ T cell differentiation and dysfunction in cancer. *Nat. Rev. Immunol.* **22**, 209–223 (2022).
- Scott, A. C. et al. TOX is a critical regulator of tumour-specific T cell differentiation. *Nature* **571**, 270–274 (2019).
- Okazaki, T. et al. PD-1 and LAG-3 inhibitory co-receptors act synergistically to prevent autoimmunity in mice. *J. Exp. Med.* **208**, 395–407 (2011).
- Ahn, E. et al. Role of PD-1 during effector CD8 T cell differentiation. *Proc. Natl Acad. Sci. USA* **115**, 4749–4754 (2018).

20. Wherry, E. J., Blattman, J. N., Murali-Krishna, K., van der Most, R. & Ahmed, R. Viral persistence alters CD8 T cell immunodominance and tissue distribution and results in distinct stages of functional impairment. *J. Virol.* **77**, 4911–4927 (2003).
21. Buenrostro, J. D., Giresi, P. G., Zaba, L. C., Chang, H. Y. & Greenleaf, W. J. Transposition of native chromatin for fast and sensitive epigenomic profiling of open chromatin, DNA-binding proteins and nucleosome position. *Nat. Methods* **10**, 1213–1218 (2013).
22. Sen, D. R. et al. The epigenetic landscape of T cell exhaustion. *Science* **354**, 1165–1169 (2016).
23. Pauken, K. E. et al. Epigenetic stability of exhausted T cells limits durability of reinvigoration by PD-1 blockade. *Science* **354**, 1160–1165 (2016).
24. Scott-Browne, J. P. et al. Dynamic changes in chromatin accessibility occur in CD8⁺ T cells responding to viral infection. *Immunity* **45**, 1327–1340 (2016).
25. Schep, A. N., Wu, B., Buenrostro, J. D. & Greenleaf, W. J. chromVAR: inferring transcription-factor-associated accessibility from single-cell epigenomic data. *Nat. Methods* **14**, 975–978 (2017).
26. Deng, W. et al. Recombinant Listeria promotes tumor rejection by CD8⁺ T cell-dependent remodeling of the tumor microenvironment. *Proc. Natl Acad. Sci. USA* **115**, 8179–8184 (2018).
27. Harty, J. T., Tvinnereim, A. R. & White, D. W. CD8⁺ T cell effector mechanisms in resistance to infection. *Annu. Rev. Immunol.* **18**, 275–308 (2000).
28. Sadler, A. J. & Williams, B. R. Interferon-inducible antiviral effectors. *Nat. Rev. Immunol.* **8**, 559–568 (2008).
29. Martinez, G. J. et al. The transcription factor NFAT promotes exhaustion of activated CD8⁺ T cells. *Immunity* **42**, 265–278 (2015).
30. Chapman, N. M., Boothby, M. R. & Chi, H. Metabolic coordination of T cell quiescence and activation. *Nat. Rev. Immunol.* **20**, 55–70 (2020).
31. Tsao, H. W. et al. Batf-mediated epigenetic control of effector CD8⁺ T cell differentiation. *Sci. Immunol.* **7**, eabi4919 (2022).
32. Yang, C. Y. et al. The transcriptional regulators Id2 and Id3 control the formation of distinct memory CD8⁺ T cell subsets. *Nat. Immunol.* **12**, 1221–1229 (2011).
33. Roychoudhuri, R. et al. BACH2 regulates CD8⁺ T cell differentiation by controlling access of AP-1 factors to enhancers. *Nat. Immunol.* **17**, 851–860 (2016).
34. Machlab, D. et al. monaLisa: an R/Bioconductor package for identifying regulatory motifs. *Bioinformatics* **38**, 2624–2625 (2022).
35. Intlekofer, A. M. et al. Anomalous type 17 response to viral infection by CD8⁺ T cells lacking T-bet and eomesodermin. *Science* **321**, 408–411 (2008).
36. Intlekofer, A. M. et al. Effector and memory CD8⁺ T cell fate coupled by T-bet and eomesodermin. *Nat. Immunol.* **6**, 1236–1244 (2005).
37. Sullivan, B. M., Juedes, A., Szabo, S. J., von Herrath, M. & Glimcher, L. H. Antigen-driven effector CD8 T cell function regulated by T-bet. *Proc. Natl Acad. Sci. USA* **100**, 15818–15823 (2003).
38. Pearce, E. L. et al. Control of effector CD8⁺ T cell function by the transcription factor Eomesodermin. *Science* **302**, 1041–1043 (2003).
39. He, R. et al. Follicular CXCR5-expressing CD8⁺ T cells curtail chronic viral infection. *Nature* **537**, 412–428 (2016).
40. Im, S. J. et al. Defining CD8⁺ T cells that provide the proliferative burst after PD-1 therapy. *Nature* **537**, 417–421 (2016).
41. Utzschneider, D. T. et al. T cell factor 1-expressing memory-like CD8⁺ T cells sustain the immune response to chronic viral infections. *Immunity* **45**, 415–427 (2016).
42. Wu, T. et al. The TCF1-Bcl6 axis counteracts type I interferon to repress exhaustion and maintain T cell stemness. *Sci. Immunol.* **1**, eaai8593 (2016).
43. Abdel-Hakeem, M. S. et al. Epigenetic scarring of exhausted T cells hinders memory differentiation upon eliminating chronic antigenic stimulation. *Nat. Immunol.* **22**, 1008–1019 (2021).
44. Hensel, N. et al. Memory-like HCV-specific CD8⁺ T cells retain a molecular scar after cure of chronic HCV infection. *Nat. Immunol.* **22**, 229–239 (2021).
45. Yates, K. B. et al. Epigenetic scars of CD8⁺ T cell exhaustion persist after cure of chronic infection in humans. *Nat. Immunol.* **22**, 1020–1029 (2021).
46. Liu, J. et al. CTCF mediates CD8⁺ effector differentiation through dynamic redistribution and genomic reorganization. *J. Exp. Med.* **220**, e20221288 (2023).
47. Amezquita, R. A. marge: an API for analysis of motifs using HOMER in R. Preprint at bioRxiv <https://doi.org/10.1101/249268> (2019).
48. Cao, Z., Sun, X., Icli, B., Wara, A. K. & Feinberg, M. W. Role of Kruppel-like factors in leukocyte development, function, and disease. *Blood* **116**, 4404–4414 (2010).
49. Yamada, T., Park, C. S., Mamkinin, M. & Lacorazza, H. D. Transcription factor ELF4 controls the proliferation and homing of CD8⁺ T cells via the Kruppel-like factors KLF4 and KLF2. *Nat. Immunol.* **10**, 618–626 (2009).
50. Guan, T. et al. ZEB1, ZEB2, and the miR-200 family form a counterregulatory network to regulate CD8⁺ T cell fates. *J. Exp. Med.* **215**, 1153–1168 (2018).
51. Omilusik, K. D. et al. Transcriptional repressor ZEB2 promotes terminal differentiation of CD8⁺ effector and memory T cell populations during infection. *J. Exp. Med.* **212**, 2027–2039 (2015).
52. Scott, C. L. & Omilusik, K. D. ZEBs: novel players in immune cell development and function. *Trends Immunol.* **40**, 431–446 (2019).
53. Shih, H. Y. et al. Developmental acquisition of regulomes underlies innate lymphoid cell functionality. *Cell* **165**, 1120–1133 (2016).
54. Hernandez, J., Aung, S., Marquardt, K. & Sherman, L. A. Uncoupling of proliferative potential and gain of effector function by CD8⁺ T cells responding to self-antigens. *J. Exp. Med.* **196**, 323–333 (2002).
55. Curtsinger, J. M., Lins, D. C. & Mescher, M. F. Signal 3 determines tolerance versus full activation of naive CD8 T cells: dissociating proliferation and development of effector function. *J. Exp. Med.* **197**, 1141–1151 (2003).
56. Otten, G. R. & Germain, R. N. Split anergy in a CD8⁺ T cell: receptor-dependent cytotoxicity in the absence of interleukin-2 production. *Science* **251**, 1228–1231 (1991).
57. Utzschneider, D. T. et al. Early precursor T cells establish and propagate T cell exhaustion in chronic infection. *Nat. Immunol.* **21**, 1256–1266 (2020).
58. Wherry, E. J. et al. Molecular signature of CD8⁺ T cell exhaustion during chronic viral infection. *Immunity* **27**, 670–684 (2007).

Publisher's note Springer Nature remains neutral with regard to jurisdictional claims in published maps and institutional affiliations.

Springer Nature or its licensor (e.g. a society or other partner) holds exclusive rights to this article under a publishing agreement with the author(s) or other rightsholder(s); author self-archiving of the accepted manuscript version of this article is solely governed by the terms of such publishing agreement and applicable law.

© The Author(s), under exclusive licence to Springer Nature America, Inc. 2023

Methods

Mice

TCR_{TAG} transgenic mice (B6.Cg-Tg(TcraY1,TcrbY1)416Tev/J)⁵⁹, TCR-OT1 (C57BL/6-Tg(TcraTcrb)1100Mjb/J), Ly5.1 (B6.SJL-Ptprca Pepcb/BoyJ), Alb-Cre (B6.Cg-Tg(Alb-cre)21Mgn/J) and C57BL/6J Thy1.1 mice were purchased from The Jackson Laboratory. TCR_{TAG};Thy1.1 double transgenic mice were generated by crossing Thy1.1 mice to TCR_{TAG} mice. TCR_{OVA};Ly5.1 double transgenic mice were generated by crossing the TCR-OT1 mice with Ly5.1 mice. ASTxAlb-Cre¹⁵ double transgenic mice were generated by crossing AST (Albumin-floxStop-SV40 large T antigen (TAG))⁶⁰ with Alb-Cre mice. ASTxAlb-Cre were used between 9 and 12 weeks of age, at which time all mice had established liver tumors. Both female and male mice were used for studies. T cell donor mice were between 6 and 10 weeks of age and were matched by sex to male and female C57BL/6 and ASTxAlb-Cre recipients. All mice were bred and housed in the animal facility at Vanderbilt University Medical Center (VUMC). Mice were on 12-h light–dark cycles. The mouse housing facility was maintained at 20–25 °C and 30–70% humidity. All animal experiments were performed in compliance with VUMC Institutional Animal Care and Use Committee (IACUC) regulations and in accordance with approved VUMC IACUC protocol M1700166-01.

Adoptive T cell transfer in acute infection and tumor models

C57BL/6 mice were inoculated intravenously with 5×10^6 or 10×10^6 colony forming units LM Δ actA Δ inlB strain⁶¹ expressing the TAG-I epitope (SAINNYAQKL, SV40 large T antigen 206–215; Aduro Biotech) or the OVA epitope (SIINFEKL), respectively, 6–12 h before T cell adoptive transfer for generation of effectors. Spleens from naive TCR_{TAG};Thy1.1 mice were mechanically disrupted with the back of a 3-ml syringe and filtered through a 70- μ m strainer into ammonium chloride potassium (ACK) buffer to lyse erythrocytes. Cells were washed twice with cold serum-free RPMI 1640 media and 2.5×10^6 TCR_{TAG};Thy1.1 CD8⁺ T cells were adoptively transferred into C57BL/6 (Thy1.2) mice inoculated with LM_{TAG} or ASTxAlb-Cre tumor-bearing mice. For OTI experiments, 2.5×10^6 TCR_{OVA};Ly5.1 splenocytes were prepared in the same manner from OTI;Ly5.1 mice and adoptively transferred into mice inoculated with LM_{OVA} or mice bearing B16-OVA lung tumors. For CFSE labeling studies, splenocytes were resuspended after the first wash in 2.5 ml of plain, serum-free RPMI 1640, rapidly mixed with equal volumes of 2× CFSE 10 μ M solution, incubated for 5 min at 37 °C at a final CFSE 5 μ M, quenched by mixing CFSE/cell solution with an equal volume of pure FBS, washed twice with serum-free RPMI, and resuspended in serum-free RPMI for transfer.

B16-OVA production and lung metastasis

The B16-F10 mouse melanoma cell line was obtained from the American Type Culture Collection (ATCC; CRL-6475). B16-OVA expressing cell line was produced by transduction with pMFG-OVAx2-EGFP overexpression vector. Briefly, pMFG-EGFP was linearized with Ncol and ligated with OVAx2 (SIINFEKL-AAY-SIINFEKL) containing oligonucleotide (IDT). Cloned constructs were sequence verified. Phoenix-AMPHO (ATCC, CRL-3213) packaging cells were transfected with pMFG-OVAx2-EGFP in calcium phosphate and B16-F10 was transduced with viral supernatant. B16-OVA cells were sorted by EGFP expression for freeze downs and culturing. B16-OVA cells were cultured in DMEM supplemented with 10% FBS and L-glutamine (cDMEM) at 37 °C in a 5% CO₂ humidified incubator. For inoculation of lung metastasis, B16-OVA was harvested at 60–80% confluence. Medium was replaced with fresh cDMEM the day before collection. Cells were washed twice with ice-cold serum-free RPMI and $2–4 \times 10^5$ cells were injected by tail vein into B6 mice. Tumors were allowed to grow for 3 weeks before T cell transfer experiments. The maximal tumor size permitted for transplantable tumors as per our VUMC IACUC-approved protocol is 3 cm in maximum diameter. No tumors in this study exceeded the maximal allowed tumor size.

Cell isolation for subsequent analyses

Spleens from experimental mice were mechanically disrupted with the back of a 3-ml syringe and filtered through a 70- μ m strainer into ACK buffer. Cells were washed once and resuspended in cold RPMI 1640 supplemented with 2 μ M glutamine, 100 U ml⁻¹ penicillin–streptomycin and 10% FBS (cRPMI). Liver tissue was mechanically disrupted using a 150- μ m metal mesh and glass pestle in ice-cold 2% FBS/PBS and passed through a 70- μ m strainer. Liver homogenate was centrifuged at 400g for 5 min at 4 °C and supernatant discarded. Liver pellet was resuspended in 20 ml of 2% FBS/PBS buffer containing 500 U heparin, mixed with 13 ml of Percoll (GE) by inversion, and centrifuged at 500g for 10 min at 4 °C. Supernatant was discarded and pellet was suspended in red blood cell lysis ACK buffer and resuspended in cRPMI for downstream applications. Periportal and celiac lymph nodes were collected and pooled for tumor-draining lymph node analysis. Lymph nodes were mechanically dissociated into single-cell solutions using the textured surface of two frosted microscope slides into ice-cold cRPMI.

Intracellular cytokine staining and transcription factor staining

Intracellular cytokine staining was performed with the Foxp3/Transcription Factor Staining Buffer Kit (Tonbo) according to the manufacturer's instructions. Briefly, T cells were mixed with 2×10^6 C57BL/6 splenocytes and stimulated with 0.5 μ g ml⁻¹ of TAG epitope I peptide in cRPMI for 4 h at 37 °C in the presence of brefeldin A (BioLegend). Where indicated, stimulation media contained anti-CD107a. Following peptide stimulation, cells were stained with for surface markers, fixed, permeabilized and stained for IFN- γ , TNF, perforin and granzyme B. Intracellular TF staining was performed with the Foxp3/Transcription Factor Staining Buffer Kit (Tonbo) according to the manufacturer's instructions

Flow cytometry and flow sorting

All flow analysis was performed on the Attune NXT Acoustic Focusing Cytometer (Thermo Fisher Scientific). The following fluorochrome-conjugated antibodies were used in analysis. The clone is denoted in parentheses.

- Anti-CD8-BV605 (53-6.7), BioLegend, 100744, B318405, dilution 1:250;
- Anti-CD8-PE (53-6.7), Tonbo, 50-0081-U100, C0081013017503, dilution 1:800;
- Anti-CD44-PCP-Cy5.5 (IM7), Tonbo, 65-0441-U100, C0441070121653, dilution 1:200;
- Anti-CD44-FITC (IM7), BioLegend, 103006, B228504, dilution 1:200;
- Anti-CD44-APC (IM7), Tonbo, 20-0441-U100, C0441022119203, dilution 1:200;
- Anti-CD44-AF700 (IM7), eBioscience, 56-0441-80, 1995539, dilution 1:200;
- Anti-CD62L-BV785 (MEL-14), BioLegend, 104440, B340191, dilution 1:200;
- Anti-CD69-PE-Cy7 (H1.2F3), eBioscience, 25-0691-82, 1981586, dilution 1:200;
- Anti-CD90.1-BV421(OX-7), BioLegend, 202529, B305864, dilution 1:1,000;
- Anti-CD90.1-PCP-Cy5.5(HIS51), eBioscience, 45-0900-80, 2227596 dilution 1:800;
- Anti-CD90.1-APC(HIS51), eBioscience, 17-0900-82, 2162254, dilution 1:800;
- Anti-CD90.1-APC-eF780 (HIS51), eBioscience, 17-0900-82, 2142928, dilution 1:800;
- Anti-CD127-FITC (A7R34), BioLegend, 135007, B255262, dilution 1:200;
- Anti-CD107a/LAMP1-FITC (ID4B), BioLegend, 121606, B283798, dilution 1:400;

Anti-GZMB-PE-Cy7 (GB11), BioLegend, 372214, 2361830, dilution 1:200;
 Anti-GZMB-AF647 (GB11), BioLegend, 515406, B341642, dilution 1:200;
 Anti-IFN- γ -BV421 (XMG1.2), BioLegend, 505829, B335329, dilution 1:400;
 Anti-IFN- γ -PE-Cy7 (XMG1.2), BioLegend, 505825, B334480, dilution 1:1,000;
 Anti-IFN- γ -APC (XMG.12), BioLegend, 505810, B290393, dilution 1:800;
 Anti-LAG3/CD223-PE (eBioC9B7W), BioLegend, 12-2231-83, 2229141, dilution 1:200;
 Anti-PD-1/CD279-PCP-eF710 (RMP1-30), eBioscience, 46-9981-80, 2294181, dilution 1:200;
 Anti-PD-1/CD279-APC (RMP1-30), BioLegend, 109112, B309096, dilution 1:200;
 Anti-TCF1-AF647 (C63D9), Cell Signaling Technology, 6709S, 12, dilution 1:400;
 Anti-TNF-PE (MP6-XT22), Life, 12-7321-82, 2124591, dilution 1:600;
 Anti-TOX-PE (REA473), Miltenyl Biotec, 130-120-716, 5220109273, dilution 1:200.

The following fluorescent cell dyes were used in the analysis.

CFSE, Tonbo, 13-0850, D0850042721, 5 μ M;
 DAPI, BioLegend, 422801, B234813, 50 ng ml $^{-1}$;
 Ghost Dye Violet 450 Viability Dye, Tonbo, 13-0863-T500, D0868083018133, dilution 1:1,000;
 Ghost Dye Red 780 Viability Dye, Tonbo, 13-0865-T500, D0871072021133, dilution 1:2,000.

Data were analyzed using FlowJo v.10.8.1 (Tree Star). Cell sorting was performed using the BD FACS Aria III (BD Biosciences) at the VUMC Flow Cytometry Shared Resource Core with BD FACSDiva Software. For pre-parking and post-parking analyses, target populations were enriched from spleens or malignant livers with CD8 negative selection kit before cell sorting workflows, (StemCell Technologies, 19853) according to the manufacturer's instructions.

RNA sequencing

ACK lysed single-cell suspensions from livers and spleens were processed as described above using sterile technique and stained with antibodies against CD8, CD90.1 and CD69 and DAPI for dead cell exclusion. Around 5,000 cells were sorted directly into TRIzol LS and frozen. Total RNA was extracted from sorted cells using the RNeasy Micro kit (Qiagen) and amplified using the SMART-Seq v4 UltraLow Input RNA Kit (Clontech). The cDNA was quantified and analyzed on the BioAnalyzer. Libraries were prepared using 7.7–300 ng of cDNA and the NEB DNA Ultra II kit. Each library was quantified after PCR and run on the Caliper GX to assess each library profile. A final quality-control assay consisting of qPCR was completed for each sample. The libraries were sequenced using the NovaSeq 6000 with 150-bp paired-end reads targeting 50 M reads per sample. RTA (v2.4.11; Illumina) was used for base calling and analysis was completed using MultiQC v1.7.5.

ATAC sequencing

Profiling of chromatin was performed by ATAC-seq as previously described²⁵. ACK lysed single-cell suspensions from livers and spleens were processed as described above using sterile technique and stained with antibodies against CD8, CD90.1 and CD69 and DAPI for dead cell exclusion. Between 1,000 and 20,000 cells were sorted into cold FCS, dimethylsulfoxide was added to 10%, and cells were frozen. Frozen T cells were then thawed and washed in cold PBS and lysed. The transposition reaction was incubated at 42 °C for 45 min. The DNA was cleaned with the MinElute PCR Purification Kit (Qiagen), and material was amplified for five cycles. After evaluation by real-time PCR, 7–13 additional PCR cycles were done. The final product was cleaned by AMPure XP beads (Beckman Coulter) at a 1× ratio, and size selection was

performed at a 0.5× ratio. Libraries were sequenced on a HiSeq 2500 or HiSeq 4000 in a 50-bp/50-bp paired-end run using the TruSeq SBS Kit v4, HiSeq Rapid SBS Kit v2 or HiSeq 3000/4000 SBS Kit (Illumina).

Bioinformatics methods

The quality of the sequenced reads was assessed with FastQC⁶² and QoRTs⁶³ (for RNA-seq samples). Unless otherwise stated, plots involving high-throughput sequencing data were created using R (v4.1.0)⁶⁴ and ggplot2 (ref. 65).

RNA-seq data analysis

Adaptors were trimmed from raw sequencing reads with TrimGalore v0.5.0 (http://www.bioinformatics.babraham.ac.uk/projects/trim_galore/) and Cutadapt (v2.8)⁶⁶. Trimmed reads were mapped with STAR (v2.7.6a)⁶⁷ to the mouse reference genome (GRCm38.p6). Fragments per gene were counted with featureCounts (v2.0.7)⁶⁸ with respect to Gencode vM25 comprehensive gene annotations. DEGs were identified using DESeq2 (v1.34.0)⁶⁹, and only Benjamini–Hochberg-corrected P values (FDR) < 0.05 were considered statistically significant.

GSEA was performed with fgsea (v1.20.0)⁷⁰, using genes ranked on the DESeq2 Wald statistic. KEGG, HALLMARK and REACTOME gene sets were retrieved from the Broad Institute's MSigDB collections^{71,72} using msigdb (v7.5.1)⁷³. Only pathways with an FDR value < 0.05 were considered enriched.

PCA and expression heat maps were created using variance-stabilizing transformed counts generated by the DESeq2 package. Heat maps are centered and scaled by row.

ATAC-seq data analysis

Alignment and identification of open chromatin regions. Reads were aligned to the mouse reference genome (GRCm38) with BWA-backtrack⁷⁴. Post-alignment filtering was done with samtools (v1.8)⁷⁵ and Broad Institute's Picard tools (<http://broadinstitute.github.io/picard/>) to remove unmapped reads, improperly paired reads, nonunique reads and duplicates. To identify regions of open chromatin, peak calling was performed with MACS2 (v2.2.7.1)⁷⁶. Only peaks with FDR values smaller than 0.01 were retained.

ATAC-seq peak atlas creation. A unified peak atlas was created from pre-parking and post-parking samples, as well as from previously published chromatin accessibility data (GSE89308). Consensus peak sets were generated for each condition if a peak was found in at least 75% of replicates. These sets were then merged with DiffBind (v3.4.11)⁷⁷ to create an atlas of accessible peaks, which was used for downstream analyses. The peak atlas was annotated using the ChIPseeker (v1.30.3)⁷⁸ and Gencode vM25.

Differentially accessible regions. Regions where the chromatin accessibility changed between different conditions were identified with DESeq2 (v1.34.0), and only Benjamini–Hochberg-corrected P values (FDR) < 0.05 were considered statistically significant. A log₂FC (cutoff of 1.5 was used in some analyses as indicated. Hidden batch effects were estimated using the svaseq function from sva (v3.42.0)⁷⁹, and the top three surrogate variables were accounted for in DESeq2.

Motif analysis. Peaks were analyzed for TF motif enrichment using chromVAR (v1.16.0)²⁵. Motifs from the CIS-BP database⁸⁰ ('mouse_pwms_v2' from chromVARmotifs v0.2.0) were used as input, after removing TFs that with low levels of expression based on the RNA-seq data (average count per million < 5). TF accessibility deviation scores and variability were calculated by chromVAR, and z-scores of deviations of the top 30 most variable TFs were visualized in a heat map.

For identifying TF motifs enriched in differentially accessible peaks, we utilized HOMER via marge (v0.0.4)⁴⁷. HOMER was run separately on hyper-accessible or hypo-accessible peaks with the

flags --size given and --mask. Motifs enriched in hyper-accessible or hypo-accessible peaks were determined by comparing the rank differences (based on *P* value).

To compare TF motifs enriched in different peak classifications (transient, stable, reinforced, intermediate), we used the calcBinned-MotifEnrR function from monaLisa (v0.0.4)³⁴. The log₂ enrichment was plotted in a heat map if the motif was enriched in at least one category ($P < 1 \times 10^{-10}$).

Peak heat maps and genome coverage plots. Genome coverage files per replicate were normalized for differences in sequencing depth (RPGC normalization) with bamCoverage from deepTools (v3.1.0)⁸¹. Blacklisted regions were excluded (<https://github.com/Boyle-Lab/Blacklist/>). Replicates were averaged together using UCSC-tools bigWigMerge and by dividing by the number of samples. ATAC-seq heat maps were created using profileplyr (v1.10.2)⁸² and ComplexHeatmap (v2.15.1)⁸³, by binning the region ± 1 kb around the peak summits in 20-bp bins. To improve visibility, bins with read counts greater than the 75th percentile + 1.5 times the interquartile range were capped at that value.

Statistics and reproducibility

No statistical method was used to predetermine sample size, but sample sizes are similar to those reported in previous publications^{5,15,17}. No data were excluded from the analyses. The experiments were not randomized. The investigators were not blinded to allocation during experiments and outcome assessment. Statistical analysis of next-generation sequencing data is described in detail above. All other experiments and statistical analysis, including two-tailed Student's *t*-test, two-way ANOVA with post hoc Tukey test and one-sample Student's *t*-test, were performed as described using Prism 9.0 (GraphPad). Data distribution was assumed to be normal, but this was not formally tested. Composite figures and schematics were generated using Powerpoint 365 (Microsoft).

Reporting summary

Further information on research design is available in the Nature Portfolio Reporting Summary linked to this article.

Data availability

RNA-seq and ATAC-seq data have been deposited in the Gene Expression Omnibus under super-series accession number GSE209712. KEGG, Hallmark and Reactome gene sets were retrieved from the Broad Institute's MSigDB collections using msigbr v7.5.177 (<https://www.gsea-msigdb.org/gsea/msigdb/index.jsp>). Source data are provided with this paper. All other data that support the findings of this study are present in the article or are available from the corresponding author upon request.

Code availability

Code has been deposited in GitHub: <https://github.com/abcwcm/Rudloff2022>.

References

59. Staveley-O'Carroll, K. et al. In vivo ligation of CD40 enhances priming against the endogenous tumor antigen and promotes CD8⁺ T cell effector function in SV40 T antigen transgenic mice. *J. Immunol.* **171**, 697–707 (2003).
60. Stahl, S. et al. Tumor agonist peptides break tolerance and elicit effective CTL responses in an inducible mouse model of hepatocellular carcinoma. *Immunol. Lett.* **123**, 31–37 (2009).
61. Brockstedt, D. G. et al. Listeria-based cancer vaccines that segregate immunogenicity from toxicity. *Proc. Natl Acad. Sci. USA* **101**, 13832–13837 (2004).
62. Andrews, S. FastQC: a quality control tool for high throughput sequence data. <http://www.bioinformatics.babraham.ac.uk/projects/fastqc> (2010).
63. Hartley, S. W. & Mullikin, J. C. QoRTs: a comprehensive toolset for quality control and data processing of RNA-Seq experiments. *BMC Bioinformatics* **16**, 224 (2015).
64. R Core Team. R: a language and environment for statistical computing. R Foundation for Statistical Computing. <https://www.R-project.org/> (2017).
65. Wickham, H. et al. *ggplot2: Elegant Graphics for Data Analysis* (2016).
66. Martin, M. Cutadapt removes adapter sequences from high-throughput sequencing reads. *EMBnet J.* **17**, 10–12 (2011).
67. Dobin, A. et al. STAR: ultrafast universal RNA-seq aligner. *Bioinformatics* **29**, 15–21 (2013).
68. Liao, Y., Smyth, G. K. & Shi, W. featureCounts: an efficient general purpose program for assigning sequence reads to genomic features. *Bioinformatics* **30**, 923–930 (2014).
69. Love, M. I., Huber, W. & Anders, S. Moderated estimation of fold change and dispersion for RNA-seq data with DESeq2. *Genome Biol.* **15**, 550 (2014).
70. Korotkevich, G. et al. Fast gene-set enrichment analysis. Preprint at bioRxiv <https://doi.org/10.1101/060012> (2021).
71. Subramanian, A. et al. Gene set enrichment analysis: a knowledge-based approach for interpreting genome-wide expression profiles. *Proc. Natl Acad. Sci. USA* **102**, 15545–15550 (2005).
72. Liberzon, A. et al. Molecular signatures database (MSigDB) 3.0. *Bioinformatics* **27**, 1739–1740 (2011).
73. Dolgalev, I. msigdbr: MSigDB gene sets for multiple organisms in a tidy data format. R package version 7.5.1.9001 <https://igordot.github.io/msigdbr/> (2022).
74. Li, H. & Durbin, R. Fast and accurate short read alignment with Burrows–Wheeler transform. *Bioinformatics* **25**, 1754–1760 (2009).
75. Li, H. et al. The sequence alignment/map format and SAMtools. *Bioinformatics* **25**, 2078–2079 (2009).
76. Liu, T. Use model-based analysis of ChIP-seq (MACS) to analyze short reads generated by sequencing protein–DNA interactions in embryonic stem cells. *Methods Mol. Biol.* **1150**, 81–95 (2014).
77. Stark, R. & Brown, G. DiffBind: differential binding analysis of ChIP-seq peak data. <http://bioconductor.org/packages/release/bioc/html/DiffBind.html> (2011).
78. Yu, G., Wang, L. G. & He, Q. Y. ChIPseeker: an R/Bioconductor package for ChIP peak annotation, comparison and visualization. *Bioinformatics* **31**, 2382–2383 (2015).
79. Leek, J. T. et al. sva: surrogate variable analysis. R package version 3.44.0 (2022).
80. Weirauch, M. T. et al. Determination and inference of eukaryotic transcription factor sequence specificity. *Cell* **158**, 1431–1443 (2014).
81. Ramirez, F. et al. deepTools2: a next generation web server for deep-sequencing data analysis. *Nucleic Acids Res.* **44**, W160–W165 (2016).
82. Carroll, T. & Barrows, D. profileplyr: visualization and annotation of read signal over genomic ranges with profileplyr. R package version 1.12.0. (2022).
83. Gu, Z., Eils, R. & Schlesner, M. Complex heatmaps reveal patterns and correlations in multidimensional genomic data. *Bioinformatics* **32**, 2847–2849 (2016).

Acknowledgements

We thank A. Schietinger and members of the laboratory of M.P. for helpful discussions. We thank E. Chiu, A. Dave, G. Anzarova and T. Bryson for technical assistance. We thank the Vanderbilt Division of Animal Care, D. Flaherty and the VUMC Flow Cytometry Shared Resource Core, A. Jones and the Vanderbilt Technologies for Advanced Genomics (VANTAGE) Core, and A. Viale and the Sloan Kettering Integrated Genomics Operation Core (IGO). We thank P. Lauer and Aduro Biotech for providing attenuated *Listeria* strains. We thank A. Schietinger, J. C. Rathmell and J. M. Balko for critical review of the manuscript. This work was supported by the following funding

sources: V Foundation Scholar Award (to M.P.), National Institutes of Health (NIH) R37CA263614 (to M.P.), Serodino Family Adventure Allee Fund (to M.P.), Vanderbilt-Ingram Cancer Center (VICC) SPORE Career Enhancement Program (to M.P.) NIH P50CA098131, Vanderbilt Digestive Disease Research Center (VDDRC) Young Investigator and Pilot Award (to M.P.) NIH P30DK058404, Medical Scientist Training Program (MSTP) NIH T32GM007347 (to M.W.R.), NIH T32GM008554 (to N.R.F.), NIH T32CA009592 (to C.R.D.R.) and NIH T32AR059039 (to M.M.E.). The VUMC Flow Cytometry Shared Resource is supported by the VICC (NIH P30CA68485) and the VDDRC (NIH P30DK058404). VANTAGE is supported by the VICC (NIH P30CA68485), the Vanderbilt Vision Center (NIH P30EY08126) and the NIH G20RR030956. IGO is supported by NIH P30CA08748, Cycle for Survival and the Marie-Josée and Henry R. Kravis Center for Molecular Oncology.

Author contributions

M.W.R. and M.P. conceived and designed the study and analyzed and interpreted data. M.W.R. carried out experiments, assisted by N.R.F., J.J.R., C.R.D.R., M.M.E., K.A.M. and S.T.J. P.Z., F.D. and D.B. designed and performed computational analyses of RNA-seq and ATAC-seq data. M.W.R. and M.P. wrote the manuscript, with all authors contributing to the writing and providing feedback.

Competing interests

The authors declare no competing interests.

Additional information

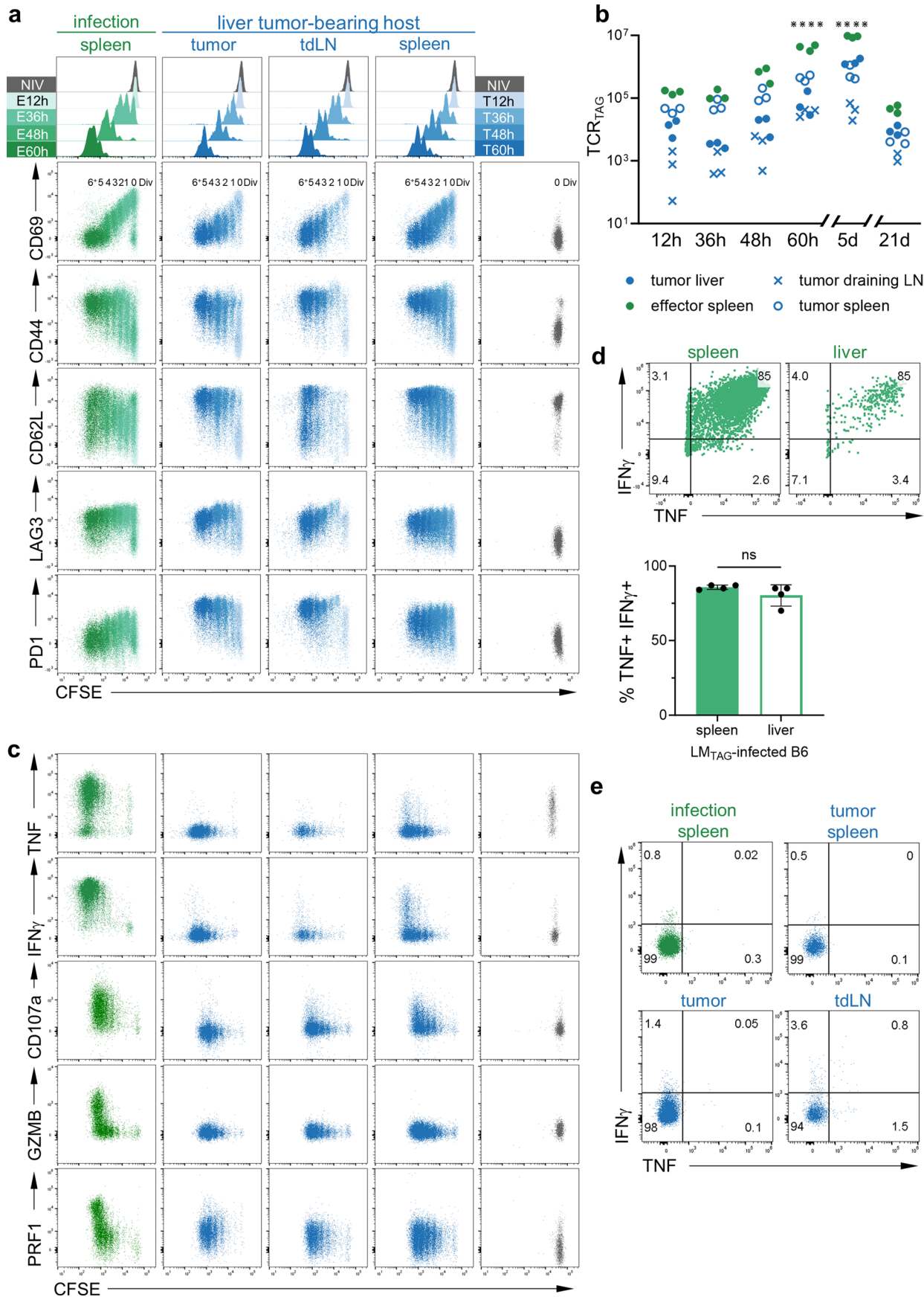
Extended data is available for this paper at <https://doi.org/10.1038/s41590-023-01578-y>.

Supplementary information The online version contains supplementary material available at <https://doi.org/10.1038/s41590-023-01578-y>.

Correspondence and requests for materials should be addressed to Mary Philip.

Peer review information *Nature Immunology* thanks Mohamed Abdel-Hakeem, Ansuman Satpathy, and the other, anonymous, reviewer(s) for their contribution to the peer review of this work. Primary Handling Editor: L. A. Dempsey, in collaboration with the *Nature Immunology* team.

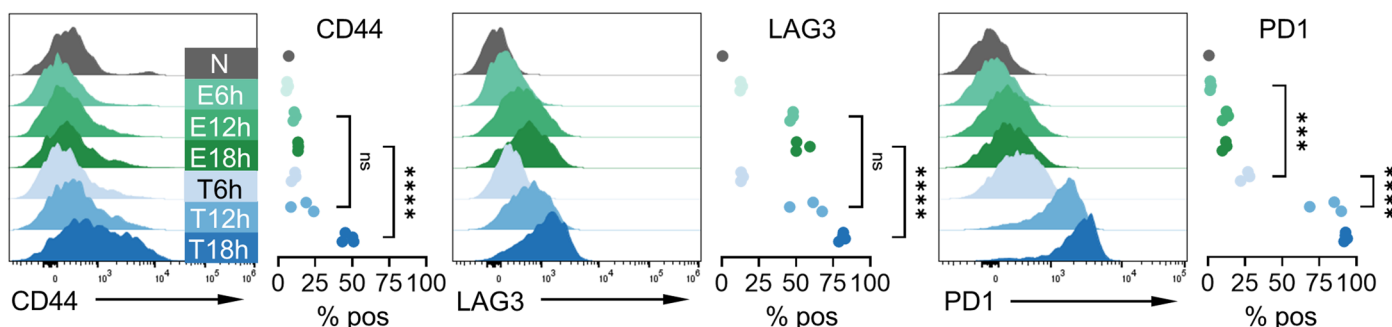
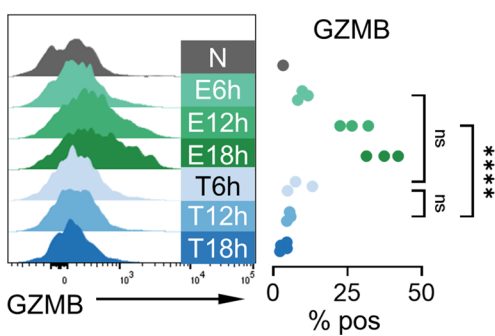
Reprints and permissions information is available at www.nature.com/reprints.



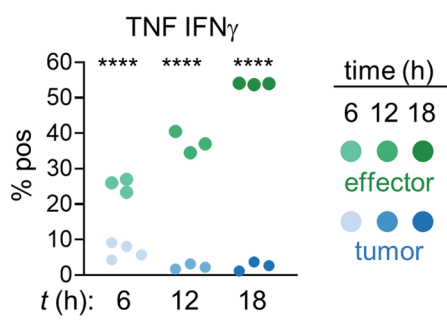
Extended Data Fig. 1 | See next page for caption.

Extended Data Fig. 1 | TST undergo robust activation and proliferation but do not gain effector function. **a**, Live CD8⁺ Thy1.1⁺ TCR_{TAG} CFSE dilution and expression of surface markers at each time point from LM_{TAG}-infected mice (spleens; green) or from tumor-bearing mice (blue), from liver tumors, tumor draining lymph nodes (tdLN), and spleens, shown together with naive *in vivo* control (N; grey). Each time point shows data concatenated from 3–4 biologic replicates. Three independent experiments were carried out with 3–4 mice/group. **b**, Counts of TCR_{TAG} per organ at 12h, 36h, 48h, and 60h as well as later time points 5 and 21+ days. Each symbol represents an individual mouse with n = 3 per group. ****P<0.0001 determined by two-way ANOVA with post hoc Šidák multiple comparison test comparing the cumulative number of TCR_{TAG} from tumor-bearing mice and infected mice. **c**, TNF, IFN γ , and CD107a production following

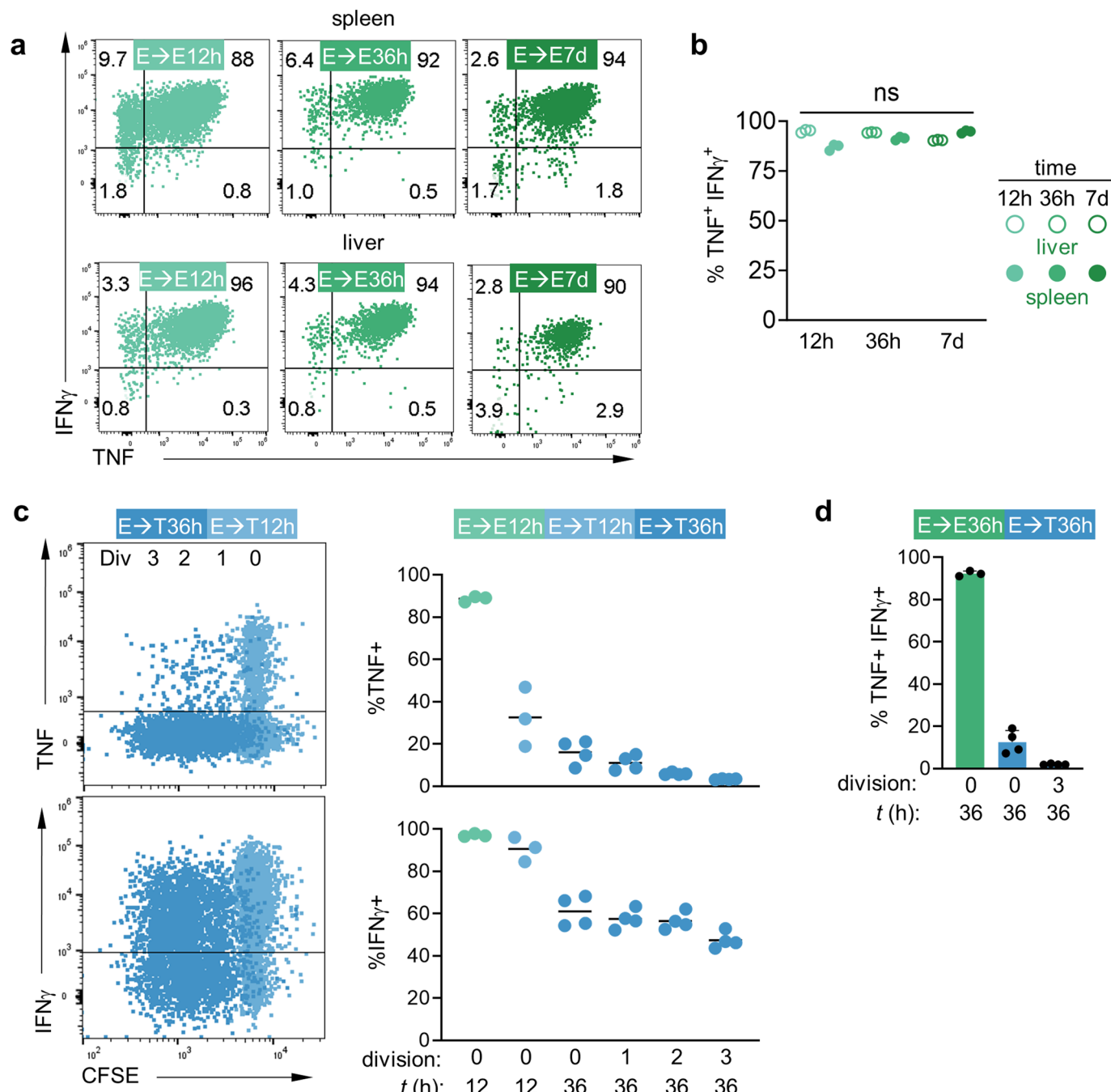
4h *ex vivo* TAG peptide stimulation in TCR_{TAG} from LM_{TAG}-infected mice (green) or from tumor-bearing mice (blue) at pooled 48 and 60h time points. GZMB and PRF1 expression was assessed immediately *ex vivo*. Naive *in vivo* TCR_{TAG} is shown for comparison (N; grey). Dot plots are concatenated from 3 mice/group. **d**, IFN γ and TNF production by TCR_{TAG} from spleens and livers of LM_{TAG}-infected mice at 48h time point following 4h *ex vivo* TAG peptide stimulation (top) and summary plot of percentage TNF⁺IFN γ ⁺ TCR_{TAG} (bottom) points where bars represent mean and error bars represent standard deviation. ns = not statistically significant, determined by unpaired two-tailed Student's t-test. **e**, Dot plots of no peptide stimulation controls from infected and tumor-bearing mice from pooled 48 and 60h time points. Two independent experiments were carried out with 2–4 mice/group.

a**b**

Extended Data Fig. 2 | Tumor-induced TST effector function impairment begins prior to cell division. Live CD8⁺ Thy1.1⁺ TCR_{TAG} analyzed from spleens of infected mice (green) and livers from tumor-bearing hosts (blue) at 6h, 12h, and 18h. **a**, Representative histograms of CD44, LAG3, and PD1 expression profiles. Two independent experiments were carried out with 3-4 mice/group. **b**, *Ex vivo* GZMB expression. Summary plots are shown to the right with each

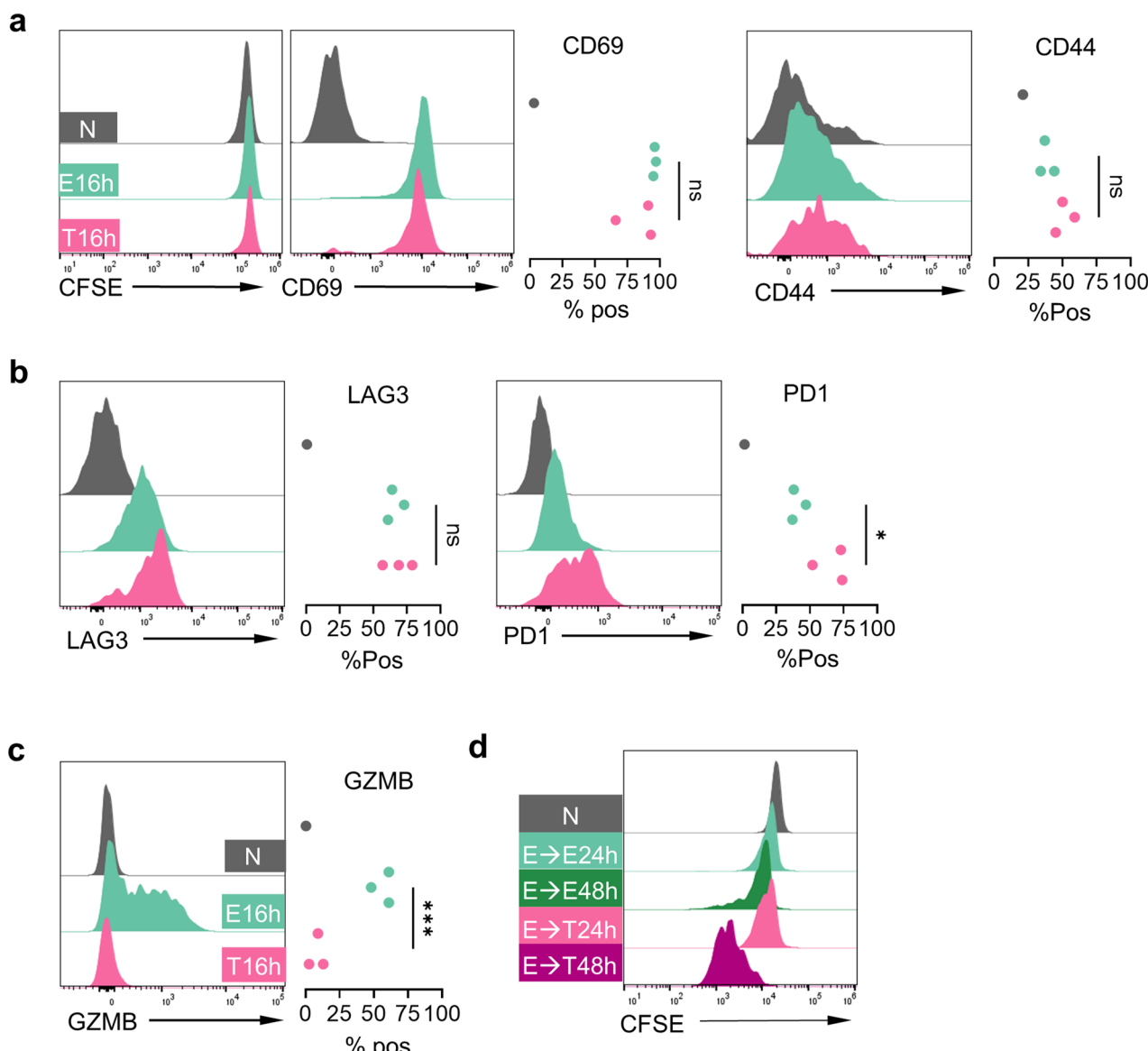
c

point representing an individual mouse and n = 3-4 per group. **c**, Independent experimental replicate of Fig. 2e showing summary plots of percentage TNF⁺IFN γ ⁺ TCR_{TAG} after peptide stimulation. Each symbol represents an individual mouse with n = 3-4 per group. ***P = 0.0003, ****P < 0.0001 determined by two-way ANOVA with post hoc Tukey test.



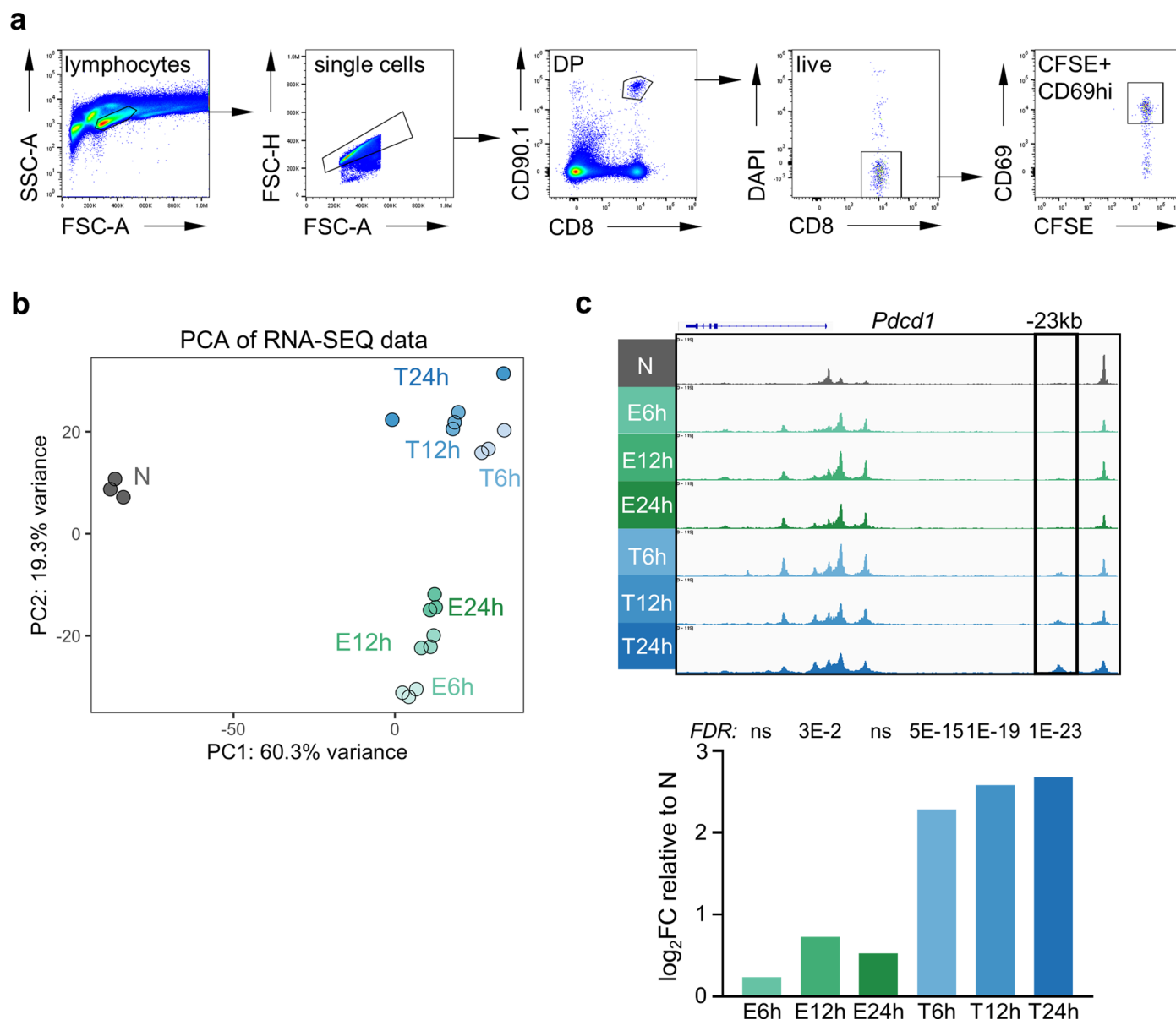
Extended Data Fig. 3 | Committed effector CD8 T cells rapidly lose function in tumor-bearing hosts. **a**, Dot plots of TCR_{TAG} TNF and IFN γ production from spleens and livers of LM^{TAG}-infected animals following 4h TAG peptide stimulation. Gates set based on no peptide stimulation controls. **b**, Summary plots of percentage TNF⁺IFN γ ⁺ TCR_{TAG} following 4h TAG peptide stimulation, where open circles represent TCR_{TAG} isolated from livers and closed circles from spleens of infected mice with n = 3 (12h, 7d) or 4 (36h) per group. Each point represents an individual animal, statistics determined by two-way ANOVA with post-hoc Tukey test. **c**, TCR_{TAG} CFSE dilution and TNF and IFN γ production at 12h

and 36h time points from tumor livers following 4h TAG peptide stimulation (left). Data is concatenated from 3-4 biological replicates/timepoint. Summary plots of percentage TNF⁺IFN γ ⁺ TCR_{TAG} (right) where each symbol represents an individual mouse with n = 3 (12h) or 4 (36h) per group and black bars represent mean. **d**, Summary plots of percentage TNF⁺IFN γ ⁺ TCR_{TAG} by cell division 36h post-transfer points where bars represent mean and error bars represent standard deviation. Each symbol represents an individual mouse with n = 3-4 per group.



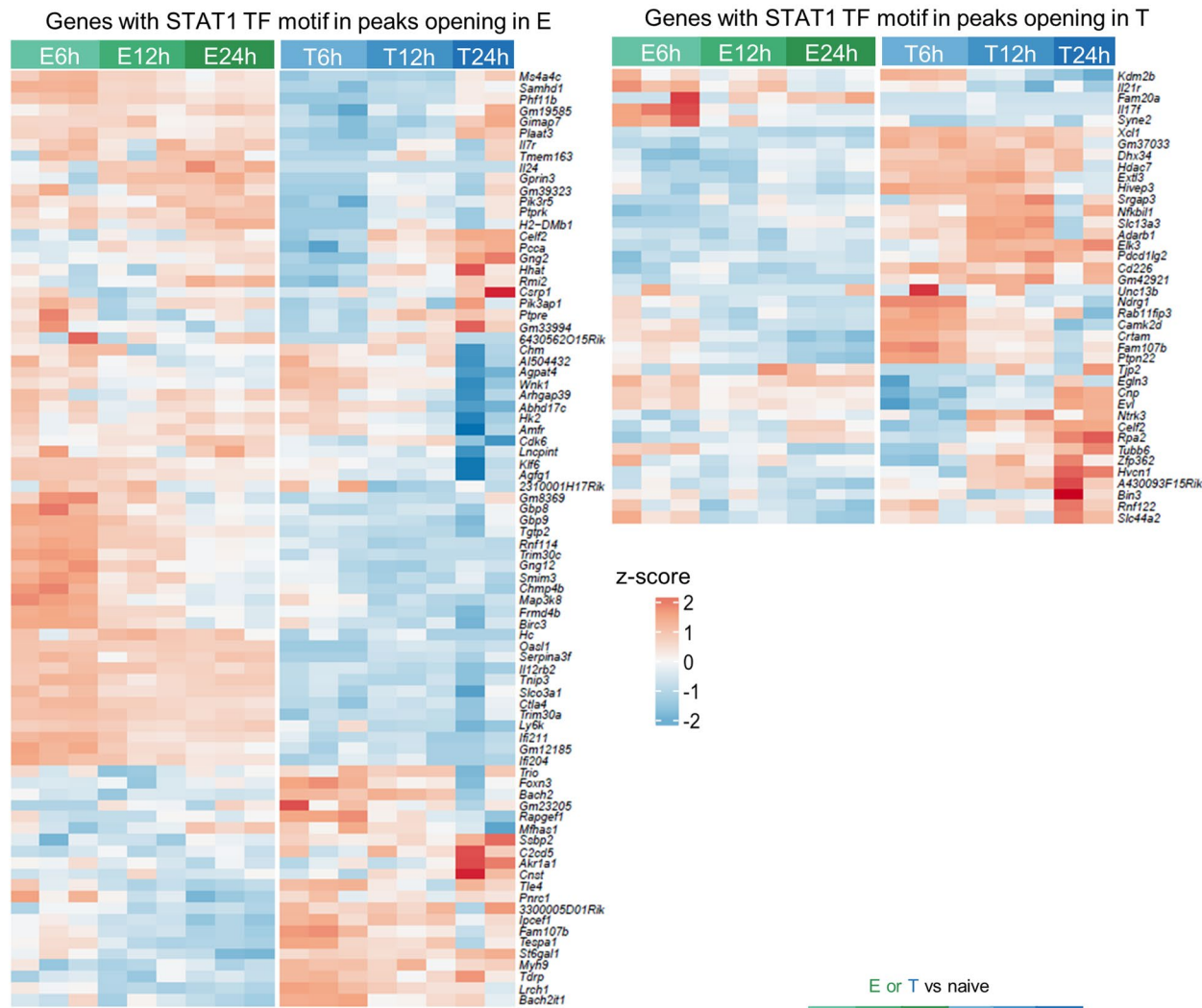
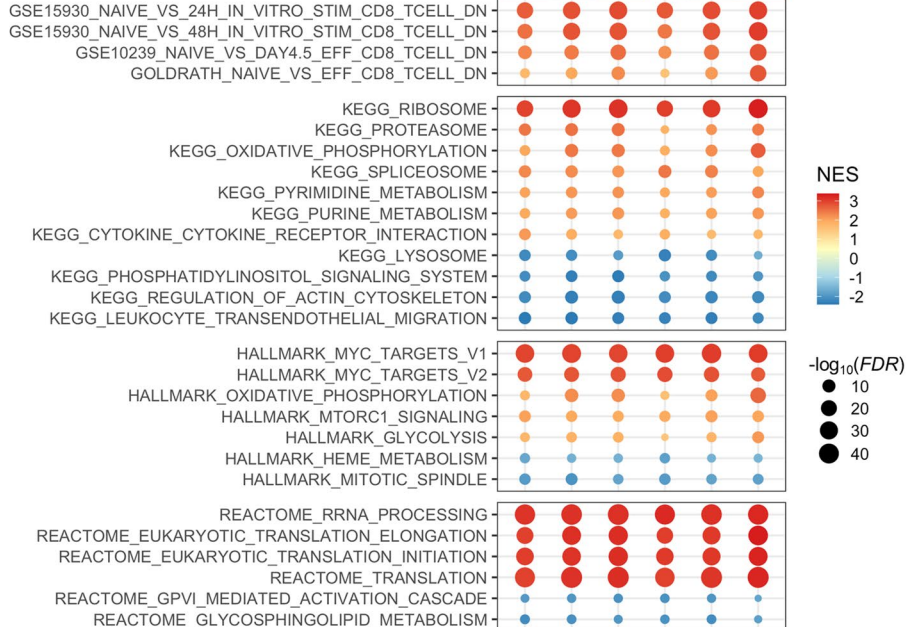
Extended Data Fig. 4 | Naive and effector TST robustly proliferate in mice with metastatic melanoma but lack effector function. Live CD8⁺ Ly5.1⁺ TCR_{OTI} analyzed from spleens of LM_{OVA} infected B6 (green) and B6 with pulmonary B16-OVA metastases (pink) at 16h. **a**, Representative histograms of CFSE, CD69, and CD44 expression profiles. **b**, Representative histograms of LAG3 and PD1 expression. **c**, *Ex vivo* GZMB expression. Summary plots are shown to the right

with each point representing an individual mouse. **d**, CFSE dilution of E5d TCR_{OTI} transferred into time-matched LM_{OVA} infected B6 (green) or B6 with pulmonary B16-OVA metastases (pink) at 24 and 48 hours following transfer. Naive TCR_{OTI} (N; grey) shown for comparison. * $P=0.0307$ and *** $P=0.0008$ determined using unpaired two-tailed Student's t-test.



Extended Data Fig. 5 | Gating strategy for sorting; dysfunction-associated epigenetic and transcriptional programming begins prior to cell division.
a, Gating strategy to sort TCR_{TAG} from infected spleens or tumor livers for sequencing studies. **b**, Principal component analysis (PCA) of RNA-SEQ data comparing top 500 most variable genes between naive (N; grey) and TCR_{TAG} differentiating during acute infection (green) and in tumors (blue) at 6, 12, 24 h

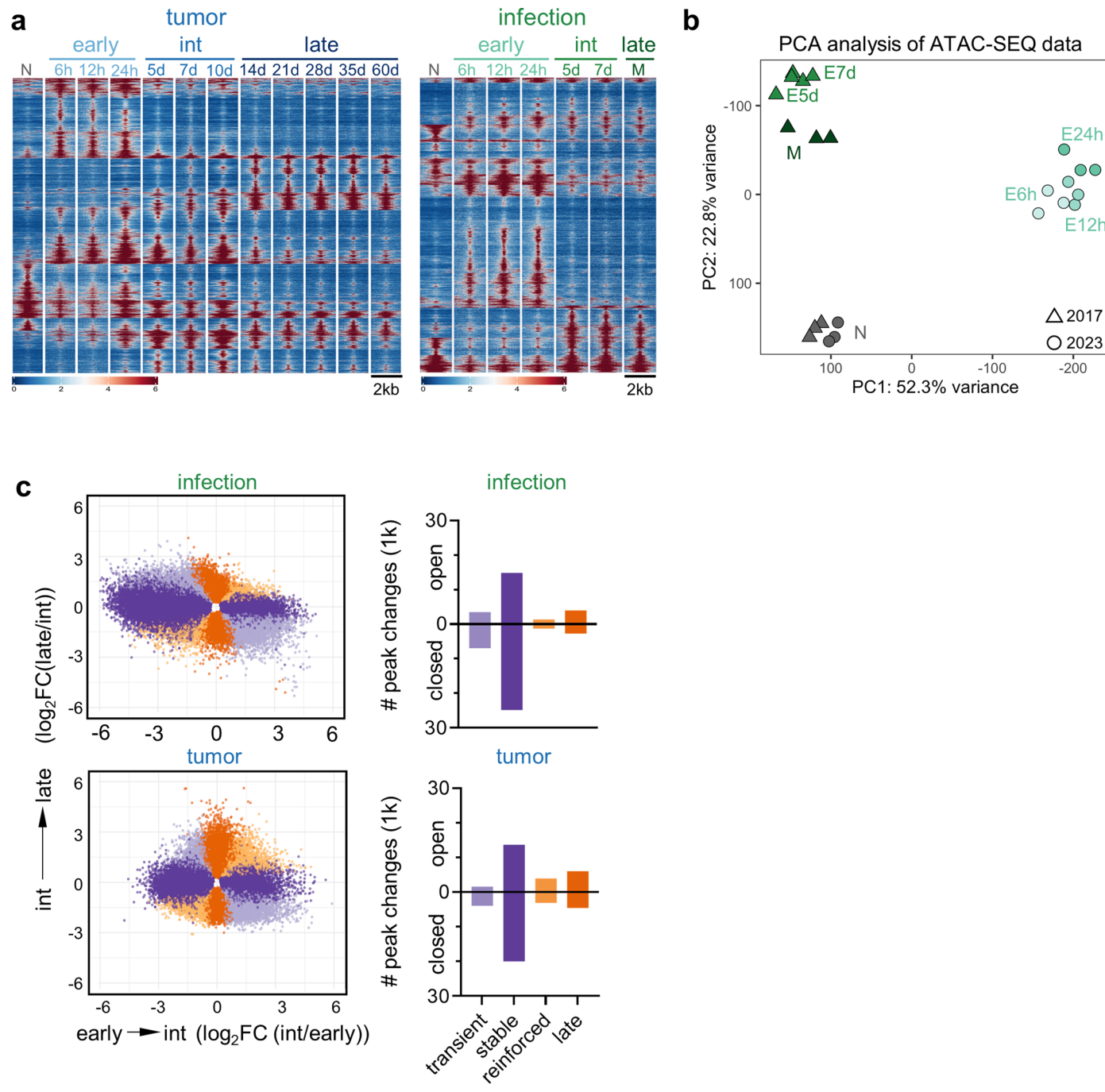
post-transfer. Each symbol represents a single biological replicate. **c**, Chromatin accessibility profile across the *Pdcd1* locus with the exhaustion-associated -23kb peak boxed (left). Summary plot (right) shows the DESeq2-determined log₂FC and FDR (two-sided Wald test with Benjamini-Hochberg correction) at the *Pdcd1* -23kb peak for early E and T time points as compared to naive (N).

a**b**

Extended Data Fig. 6 | See next page for caption.

Extended Data Fig. 6 | STAT1 motif enrichment is accompanied by increased gene expression in CD8 T cells activated during acute infection; tumor- and infection-activated CD8 T cells show similar enrichment of T cell activation-associated genes. **a**, Heatmap showing expression of differentially-expressed genes with peaks containing STAT1 motifs (by ChromVar; Fig. 5e) in effector

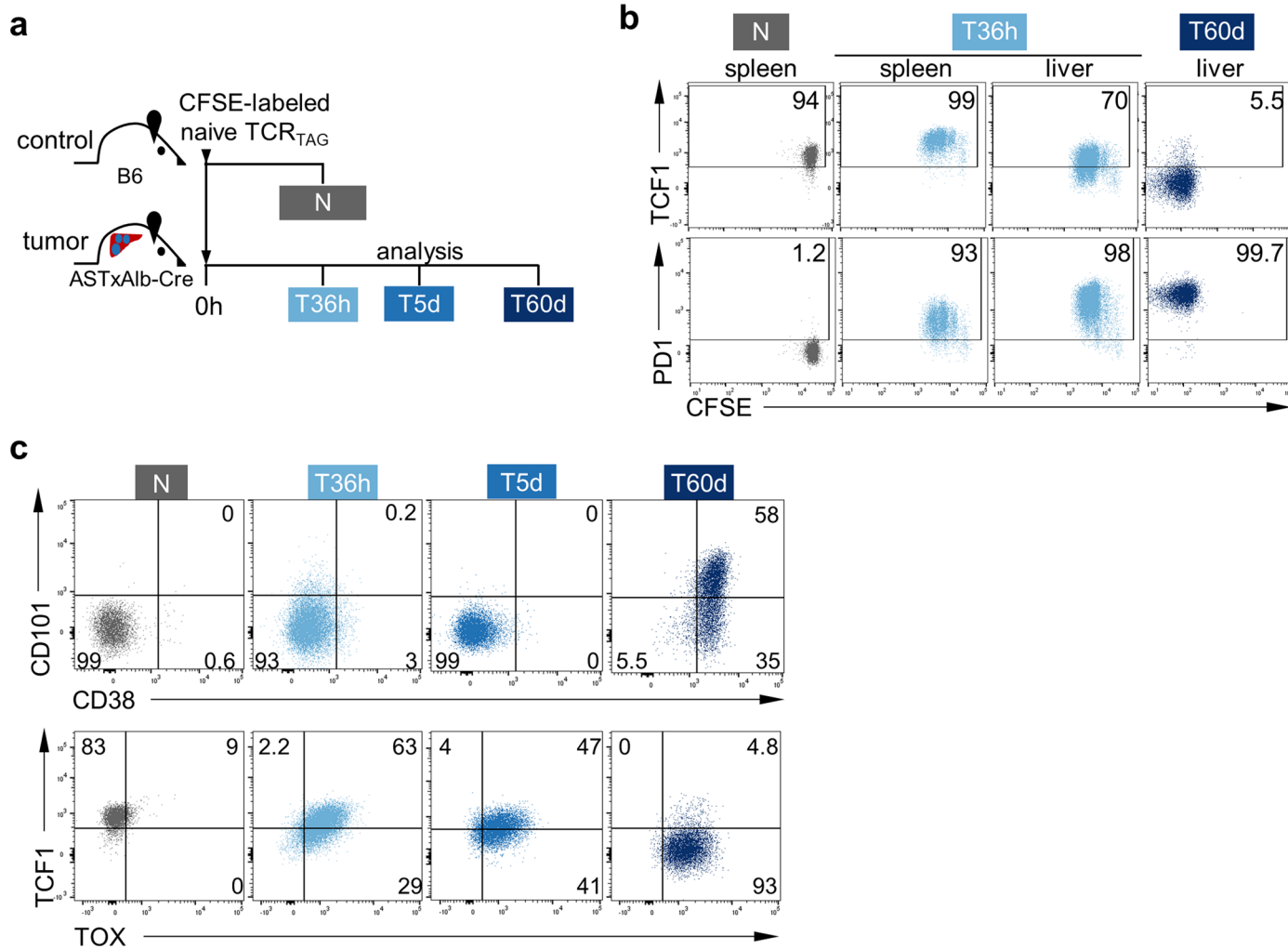
(E, left) or tumor (T, right) across time points. Heatmaps are z-score normalized across rows. **b**, Gene set enrichment analysis (GSEA) of E versus N or T versus N at 6h, 12h, and 24h post transfer for activation associated gene sets and KEGG, HALLMARK, and REACTOME gene sets. Color represents normalized enrichment score (NES) and circle size represents the negative \log_{10} (*FDR*).



Extended Data Fig. 7 | Pre-division tumor-induced TST chromatin remodeling is reinforced with time and tumor antigen exposure.

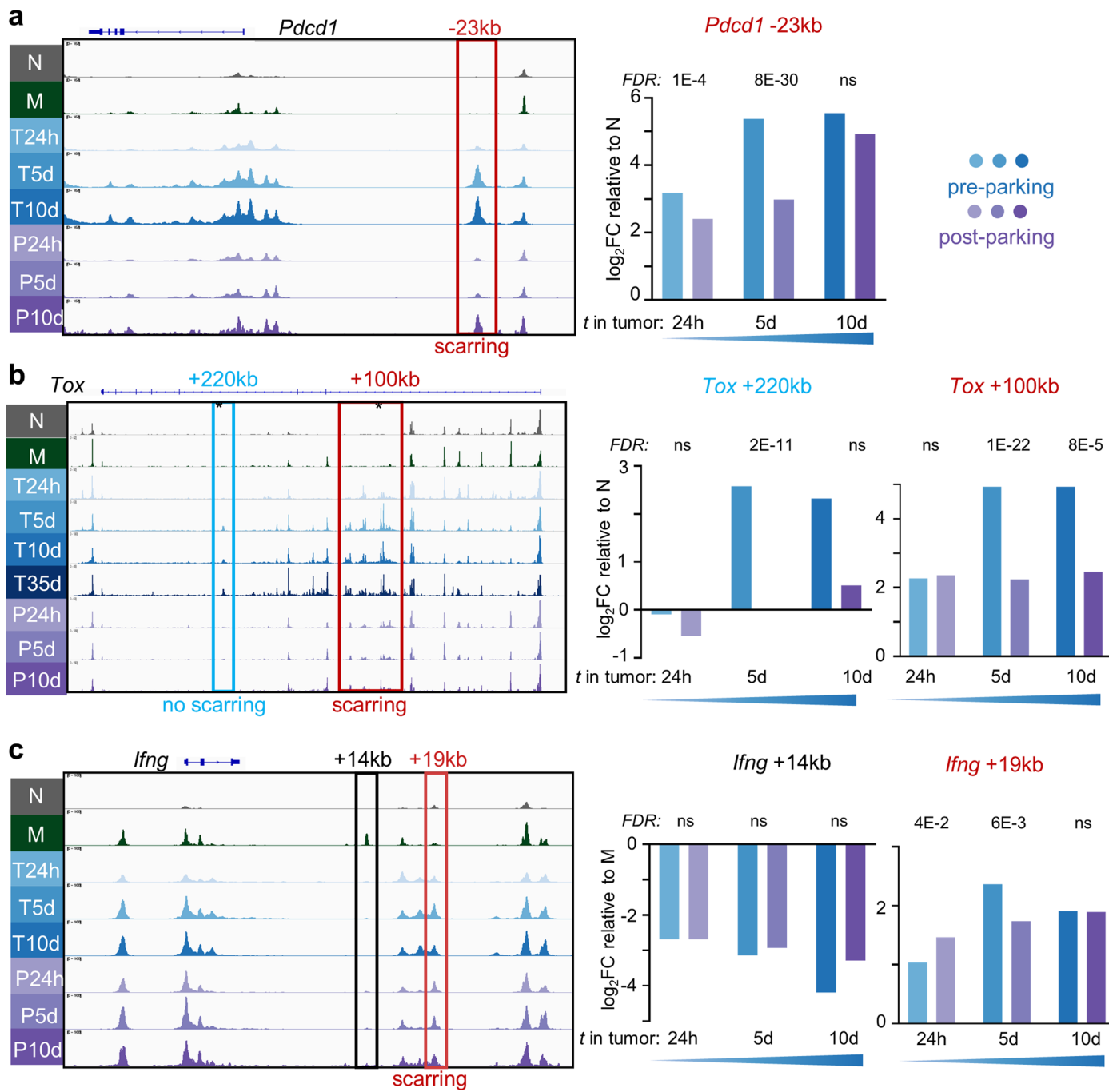
a, Chromatin accessibility heatmap showing naive (N) and TCR_{TAG} from 6h to 60+d in liver tumors of ASTxCre (left) and in LM_{TAG}-infected B6 (right). Each row represents one of 29,884 (left) or 31,756 (right) peaks (differentially accessible between at least one sequential time point comparison; $FDR < 0.05$, $|\log_2 FC| > 1.5$) displayed over 2kb window centered on the peak summit. Scale units are RPGC normalized to 1x sequencing depth for 20 bp bins with blue indicating closed chromatin and red open chromatin. Peaks are clustered by k-means ($k = 6$).

b, PCA comparing chromatin accessibility in TCR_{TAG} from 6h to M during infection. Each symbol represents a single biological replicate. **c**, Upper panel shows peak changes for early (E24h) → intermediate (E5d) transition ($\log_2 FC E5d/E24h$) versus int (E7d) → late (M) transition ($\log_2 FC M/E7d$) (upper). Lower panel shows peak changes for early (T24h) → int (T5d) transition ($\log_2 FC T5d/T24h$) versus int (T7d) → late (T14d) transition ($\log_2 FC T14d/T7d$). Each point represents an individual peak colored according to the scheme in Fig. 5c. To the right are shown corresponding bar plots showing the number of peaks in e.



Extended Data Fig. 8 | Early TST uniformly express TCF1. **a**, Experimental scheme: CFSE-labeled naive TCR_{TAG} (Thy1.1) were adoptively transferred into B6 (Thy1.2) or ASTxAlb-Cre mice (Thy1.2). TCR_{TAG} were re-isolated at 36 h (T36h), 5 d (T5d), and 60 d (T60d) from spleens and livers for flow cytometric analysis (Naive *in vivo* (N; grey); tumor (T; blue)). **b**, Dot plots of TST TCF1 and PD1 expression

by CFSE dilution across time points. **c**, Dot plots comparing CD38 and CD101 (top) or TOX and TCF1 (bottom) expression in TST isolated from tumor-bearing livers across time points. Gates set based on N with inset numbers indicating percentage of cells in each gate. Plots are concatenated from 3–4 samples/time point.



Extended Data Fig. 9 | Duration of tumor antigen exposure determines dysfunction stability and imprinting. Chromatin accessibility profiles across selected gene loci for TCR_{TAG} activated in tumor for 24h (T24h), 5d (T5d), 10d (T10d) pre-parking (blue) and post-parking (P24h, P5d, P10d) (purple) with naive (grey) and memory (green). **a**, *Pdcd1* gene locus with -23 kb enhancer peak boxed in red. Summary plot (right) shows the DESeq2-determined $\log_2\text{FC}$ and *FDR* (two-sided Wald test with Benjamini-Hochberg correction) at the *Pdcd1*-23kb peak for pre- (blue) and post-park (purple) relative to naive. **b**, *Tox* locus with blue box representing region without epigenetic scarring and red box showing region with epigenetic scarring. Star denotes representative +100 kb peak from

scar region used for quantification on right. Late dysfunctional TCR_{TAG} activated in tumor (D35) added for comparison. Summary plot (right) shows the DESeq2-determined $\log_2\text{FC}$ and *FDR* (two-sided Wald test with Benjamini-Hochberg correction) at the *Tox*+220 kb and +100 kb peaks for pre- (blue) and post-park (purple) relative to naive. **c**, *Ifng* locus with black box denoting +14kb peak open in memory but not in pre- or post-parking samples, and red box denoting +19kb peak open in both pre- and post-parking samples. Summary plot (right) shows the DESeq2-determined $\log_2\text{FC}$ and *FDR* (two-sided Wald test with Benjamini-Hochberg correction) for the *Ifng*+14kb and +19 kb peak area pre- (blue) and post-park (purple) relative to memory.

Corresponding author(s): Mary Philip

Last updated by author(s): Jul 6, 2023

Reporting Summary

Nature Portfolio wishes to improve the reproducibility of the work that we publish. This form provides structure for consistency and transparency in reporting. For further information on Nature Portfolio policies, see our [Editorial Policies](#) and the [Editorial Policy Checklist](#).

Statistics

For all statistical analyses, confirm that the following items are present in the figure legend, table legend, main text, or Methods section.

n/a Confirmed

- The exact sample size (n) for each experimental group/condition, given as a discrete number and unit of measurement
- A statement on whether measurements were taken from distinct samples or whether the same sample was measured repeatedly
- The statistical test(s) used AND whether they are one- or two-sided
Only common tests should be described solely by name; describe more complex techniques in the Methods section.
- A description of all covariates tested
- A description of any assumptions or corrections, such as tests of normality and adjustment for multiple comparisons
- A full description of the statistical parameters including central tendency (e.g. means) or other basic estimates (e.g. regression coefficient) AND variation (e.g. standard deviation) or associated estimates of uncertainty (e.g. confidence intervals)
- For null hypothesis testing, the test statistic (e.g. F , t , r) with confidence intervals, effect sizes, degrees of freedom and P value noted
Give P values as exact values whenever suitable.
- For Bayesian analysis, information on the choice of priors and Markov chain Monte Carlo settings
- For hierarchical and complex designs, identification of the appropriate level for tests and full reporting of outcomes
- Estimates of effect sizes (e.g. Cohen's d , Pearson's r), indicating how they were calculated

Our web collection on [statistics for biologists](#) contains articles on many of the points above.

Software and code

Policy information about [availability of computer code](#)

Data collection Attune Cytometric Software 5.2.2302.0 was used in data collection.

Data analysis Flow cytometry: FlowJo (v10.8.0; Treestar)
Graphs: Prism (9.2.0)
Figures: PowerPoint 365 (Microsoft)

ATAC-SEQ and RNA-SEQ: R (v4.1.0), DESeq2 (v1.32.0), samtools (v1.8), MACS2 (v2.2.7.1), DiffBind (v3.2.1), ChIPseeker (v1.30.0), sva (v3.40.0), chromVAR (v1.14.0), chromVARmotifs (v0.2.0), deepTools (v3.1), profileplyr (v1.8.0), ComplexHeatmap (v2.8.0), fgsea v1.20.0, HOMER via marge v0.0.4.

The quality of the sequenced reads was assessed with FastQC41 and QoRTs42 (for RNA-seq samples). Adaptors were trimmed from raw sequencing reads with TrimGalore v0.5.0 (http://www.bioinformatics.babraham.ac.uk/projects/trim_galore/) and Cutadapt v2.8. Trimmed reads were mapped with STAR v2.7.6a to the mouse reference genome (GRCm38.p6). Fragments per gene were counted with featureCounts v2.0.7 with respect to Gencode vM25 comprehensive gene annotations. Differentially expressed genes were identified by Wald tests using DESeq2 v1.32.0, and only Benjamini–Hochberg corrected P values < 0.05 were considered statistically significant.

Reads were aligned to the mouse reference genome (GRCm38) with BWA-backtrack49. Post alignment filtering was done with samtools v1.8 and Broad Institute's Picard tools (<http://broadinstitute.github.io/picard/>) to remove unmapped reads, improperly paired reads, nonunique reads, and duplicates. To identify regions of open chromatin, peak calling was performed with MACS2 v2.2.7.1. Only peaks with adjusted P values smaller than 0.01 were retained. Consensus peak sets were generated for tumor and infection at each transition if a peak was found in at least two replicates. Reproducible peaks at each transition were merged with DiffBind v3.2.1 to create an atlas of accessible peaks, which

was used for downstream analyses. The peak atlas was annotated using the ChIPseeker v1.30.0 and TxDb.Mmusculus.UCSC.mm10.knownGene. Regions where the chromatin accessibility changed between different conditions were identified with DESeq2 v1.32.0, and only Benjamini–Hochberg corrected P values < 0.05 were considered statistically significant. A log2fold change cutoff of 1.5 was used in some analyses as indicated. When comparing earlier time points against previously published chromatin accessibility data at later time points, hidden batch effects were estimated using the svaseq function from sva v3.40.0, and the top 3 surrogate variables were accounted for in DESeq2. Peaks were analyzed for transcription factor (TF) motif enrichment using chromVAR v1.14.0. Motifs from the CIS-BP database ('mouse_pwms_v2' from chromVARmotifs v0.2.0) were used as input, after removing TFs that were lowly expressed based on the RNA-SEQ data (average count-per-million < 10). TF accessibility deviation scores and variability were calculated by chromVAR, and z-scores of deviations of the top 30 most variable TFs were visualized in a heatmap. For identifying TF motifs enriched in differentially accessible peaks, we utilized HOMER via marge v0.0.451. HOMER was run separately on hyper- or hypo-accessible peaks with the flags -size given and -mask. Motifs enriched in hyper- or hypo-accessible peaks were determined by comparing the rank differences (based on P value). To compare TF motifs enriched in different peak classifications (transient, stable, reinforced, intermediate), we employed the calcBinnedMotifEnrR function from monaLisa v0.0.438. The log2 enrichment was plotted in a heatmap if the motif was enriched in at least one category (p < 1e-10).

Code is available on GitHub: <https://github.com/abcwcm/Rudloff2022>

For manuscripts utilizing custom algorithms or software that are central to the research but not yet described in published literature, software must be made available to editors and reviewers. We strongly encourage code deposition in a community repository (e.g. GitHub). See the Nature Portfolio [guidelines for submitting code & software](#) for further information.

Data

Policy information about [availability of data](#)

All manuscripts must include a [data availability statement](#). This statement should provide the following information, where applicable:

- Accession codes, unique identifiers, or web links for publicly available datasets
- A description of any restrictions on data availability
- For clinical datasets or third party data, please ensure that the statement adheres to our [policy](#)

All data generated and supporting the findings of this study are available within the paper. The RNA-SEQ and ATAC-SEQ data have been deposited in the Gene Expression Omnibus (GEO Super-Series accession number GSE209712).

KEGG, HALLMARK, and REACTOME gene sets were retrieved from the Broad Institute's MSigDB collections using msigbr v7.5.177 (<https://www.gsea-msigdb.org/gsea/msigdb/index.jsp>).

Human research participants

Policy information about [studies involving human research participants and Sex and Gender in Research](#).

Reporting on sex and gender	not applicable
Population characteristics	not applicable
Recruitment	not applicable
Ethics oversight	not applicable

Note that full information on the approval of the study protocol must also be provided in the manuscript.

Field-specific reporting

Please select the one below that is the best fit for your research. If you are not sure, read the appropriate sections before making your selection.

Life sciences Behavioural & social sciences Ecological, evolutionary & environmental sciences

For a reference copy of the document with all sections, see nature.com/documents/nr-reporting-summary-flat.pdf

Life sciences study design

All studies must disclose on these points even when the disclosure is negative.

Sample size	No statistical method was used to predetermine sample size, but sample sizes are similar to those reported in previous publications. Sample sizes are as indicated in the figure legends.
Data exclusions	No data were excluded.
Replication	Results were replicated with at least two independent experiments. Exact number of replicates are as indicated in figure legends.
Randomization	Age- and sex-matched animals were used for each experiment. Mice were randomly assigned to experimental groups.

Blinding was not performed due to requirements for cage labeling and animal monitoring requirements, and all data collected were strictly quantitative (flow cytometry and next generation sequencing).

Reporting for specific materials, systems and methods

We require information from authors about some types of materials, experimental systems and methods used in many studies. Here, indicate whether each material, system or method listed is relevant to your study. If you are not sure if a list item applies to your research, read the appropriate section before selecting a response.

Materials & experimental systems

n/a	Involved in the study
<input type="checkbox"/>	<input checked="" type="checkbox"/> Antibodies
<input type="checkbox"/>	<input checked="" type="checkbox"/> Eukaryotic cell lines
<input checked="" type="checkbox"/>	<input type="checkbox"/> Palaeontology and archaeology
<input type="checkbox"/>	<input checked="" type="checkbox"/> Animals and other organisms
<input checked="" type="checkbox"/>	<input type="checkbox"/> Clinical data
<input checked="" type="checkbox"/>	<input type="checkbox"/> Dual use research of concern

Methods

n/a	Involved in the study
	<input type="checkbox"/> <input checked="" type="checkbox"/> ChIP-seq
	<input type="checkbox"/> <input checked="" type="checkbox"/> Flow cytometry
	<input checked="" type="checkbox"/> <input type="checkbox"/> MRI-based neuroimaging

Antibodies

Antibodies used

The following fluorochrome-conjugated antibodies were used in analysis. Clone is denoted in parentheses.

Anti-CD8-BV605 (53-6.7), BioLegend, Cat# 100744, Lot# B318405, Dilution 1:250
 Anti-CD8-PE (53-6.7), Tonbo, Cat# 50-0081-U100, Lot# C0081013017503, Dilution 1:800
 Anti-CD44-PCP-Cy5.5 (IM7), Tonbo, Cat# 65-0441-U100, Lot# C0441070121653, Dilution 1:200
 Anti-CD44-FITC (IM7), BioLegend, Cat# 103006, Lot# B228504, Dilution 1:200
 Anti-CD44-APC (IM7), Tonbo, Cat# 20-0441-U100, Lot# C0441022119203, Dilution 1:200
 Anti-CD44-AF700 (IM7), eBioscience, Cat# 56-0441-80, Lot# 1995539, Dilution 1:200
 Anti-CD62L-BV785 (MEL-14), BioLegend, Cat# 104440, Lot# B340191, Dilution 1:200
 Anti-CD69-PE-Cy7 (H1.2F3), eBioscience, Cat# 25-0691-82, Lot# 1981586, Dilution 1:200
 Anti-CD90.1-BV421 (OX-7), BioLegend, Cat# 202529, Lot# B305864, Dilution 1:1000
 Anti-CD90.1-PCP-Cy5.5 (HIS51), eBioscience, Cat# 45-0900-80, Lot# 2227596 Dilution 1:800
 Anti-CD90.1-APC (HIS51), eBioscience, Cat# 17-0900-82, Lot# 2162254, Dilution 1:800
 Anti-CD90.1-APC-eF780 (HIS51), eBioscience, Cat# 17-0900-82, Lot# 2142928, Dilution 1:800
 Anti-CD127-FITC (A7R34), BioLegend, Cat# 135007, Lot# B255262, Dilution 1:200
 Anti-CD107a/LAMP1-FITC (ID4B), BioLegend, Cat# 121606, Lot# B283798, Dilution 1:400
 Anti-GZMB-PE-Cy7 (GB11), BioLegend, Cat# 372214, Lot# 2361830, Dilution 1:200
 Anti-GZMB-AF647 (GB11), BioLegend, Cat# 515406, Lot# B341642, Dilution 1:200
 Anti-IFNgamma-BV421 (XMG1.2), BioLegend, Cat# 505829, Lot# B335329, Dilution 1:400
 Anti-IFNgamma-PE-Cy7 (XMG1.2), BioLegend, Cat# 505825, Lot# B334480, Dilution 1:1000
 Anti-IFNgamma-APC (XMG.12), BioLegend, Cat# 505810, Lot# B290393, Dilution 1:800
 Anti-LAG3/CD223-PE (eBioC9B7W), BioLegend, Cat# 12-2231-83, Lot# 2229141, Dilution 1:200
 Anti-PD1/CD279-PCP-eF710 (RMP1-30), eBioscience, Cat# 46-9981-80, Lot# 2294181, Dilution 1:200
 Anti-PD1/CD279-APC (RMP1-30), BioLegend, Cat# 109112, Lot# B309096, Dilution 1:200
 Anti-TCF1-AF647 (C63D9), Cell Signaling Technology, Cat# 67095, Lot# 12, Dilution 1:400
 Anti-TNFAlpha-PE (MP6-XT22), Life, Cat# 12-7321-82, Lot# 2124591, Dilution 1:600
 Anti-TOX-PE (REA473), Miltenyi Biotec, Cat# 130-120-716, Lot# 5220109273, Dilution 1:200

The following fluorescent cell dyes were used in analysis.

CFSE, Tonbo, Cat# 13-0850, Lot# D0850042721, 5 uM
 DAPI, BioLegend, Cat# 422801, Lot# B234813, 50 ng/mL
 Ghost Dye Violet 450 Viability Dye, Tonbo, Cat# 13-0863-T500, Lot# D0868083018133, Dilution 1:1000
 Ghost Dye Red 780 Viability Dye, Tonbo, Cat# 13-0865-T500, Lot# D0871072021133, Dilution 1:2000

Validation

All antibodies used in this study are commercially available. Validation has been performed by manufacturer:

Biolegend (<https://www.biologegend.com/en-us/antibodies-reagents>)
 Tonbo/Cytel (<https://cytekbio.com/collections/tonbo-reagents>)
 eBioscience/ThermoFisher (<https://www.thermofisher.com/us/en/home/life-science/cell-analysis/flow-cytometry/antibodies-for-flow-cytometry.html?icid=ab-search-additional-products-flow-cytometry-antibodies-2020>)
 Cell Signaling Technology (<https://www.cellsignal.com/products/antibody-conjugates/tcf1-tcf7-c63d9-rabbit-mab-alex-fluor-647-conjugate/6709>)
 Miltenyi Biotec (<https://www.miltenyibiotec.com/US-en/products/tox-antibody-anti-human-mouse-reafinity-reaa473.html#conjugate=pe:size=100-tests-in-200-ul>)

Eukaryotic cell lines

Policy information about [cell lines and Sex and Gender in Research](#)

Cell line source(s)	B16-F10 melanoma cell line was obtained from ATCC (CRL-6475).
Authentication	ATCC carried out species authentication by COI assay. We confirmed that B16-F10 cells maintained in culture contain black melanosomes, grew in described spindle-shaped and epithelial-like pattern, and formed black-colored tumors in vivo characteristic of melanoma.
Mycoplasma contamination	Cell line tested negative for mycoplasma contamination
Commonly misidentified lines (See ICLAC register)	No commonly misidentified cell line was used in the study.

Animals and other research organisms

Policy information about [studies involving animals; ARRIVE guidelines](#) recommended for reporting animal research, and [Sex and Gender in Research](#)

Laboratory animals	All mice were bred and maintained in the specific pathogen free barrier facility at Vanderbilt University Medical Center. TCRTAG transgenic mice (B6.Cg-Tg(TcraY1,TcrbY1)416Tev/J), TCR-OT1 (C57BL/6-Tg(TcraTcrb)1100Mjb/J), Ly5.1 (B6.SJL-Ptprca Pepcb/BoyJ), Alb-Cre (B6.Cg-Tg(Alb-cre)21Mgn/J), C57BL/6J Thy1.1, and C57BL/6J Thy1.2 mice were purchased from The Jackson Laboratory. TCRTAG;Thy1.1 double transgenic mice were generated by crossing Thy1.1 mice to TCRTAG mice. TCROVA;Ly5.1 double transgenic mice were generated by crossing the TCR-OT1 mice with Ly5.1 mice. ASTxAlb-Cre double transgenic mice were generated by crossing AST (Albumin-floxStop-SV40 large T antigen (TAG)) with Alb-Cre mice. Male and female mice aged 6-12 weeks were age-and sex-matched for experiments. Mice were on 12h light-dark cycles. The mouse housing facility was maintained at 20-25C and 30-70% humidity.
Wild animals	No wild animals were used in this study.
Reporting on sex	Both male and female mice were used for experiments to address sex as a biological variable. Results reported in this study were identical in male and female mice.
Field-collected samples	No field-collected samples were used in this study.
Ethics oversight	All animal experiments were performed in compliance with VUMC Institutional Animal Care and Use Committee (IACUC) regulations and in accordance with approved VUMC IACUC protocol M1700166-01.

Note that full information on the approval of the study protocol must also be provided in the manuscript.

Flow Cytometry

Plots

Confirm that:

- The axis labels state the marker and fluorochrome used (e.g. CD4-FITC).
- The axis scales are clearly visible. Include numbers along axes only for bottom left plot of group (a 'group' is an analysis of identical markers).
- All plots are contour plots with outliers or pseudocolor plots.
- A numerical value for number of cells or percentage (with statistics) is provided.

Methodology

Sample preparation	Spleens from experimental mice were mechanically disrupted with the back of 3 mL syringe and filtered through a 70 µm strainer into ACK buffer. Cells were washed once and resuspended in cold RPMI 1640 supplemented with 2 µM glutamine, 100 U/mL penicillin/streptomycin, and 10% FBS (cRPMI). Liver tissue was mechanically disrupted using a 150 µm metal mesh and glass pestle in ice-cold 2% FBS/PBS and passed through a 70 µm strainer. Liver homogenate was centrifuged at 400g for 5 min at 4°C and supernatant discarded. Liver pellet was resuspended in 20 mL of 2% FBS/PBS buffer containing 500 U heparin, mixed with 13 mL of Percoll (GE) by inversion, and centrifuged at 500g for 10 min at 4°C. Supernatant was discarded and pellet was RBC lysed in ACK buffer and resuspended in cRPMI for downstream applications. Periportal and celiac lymph nodes were collected and pooled for tumor draining lymph node analysis. Lymph nodes were mechanically dissociated into single cell solutions using the textured surface of two frosted microscope slides into ice-cold cRPMI.
Instrument	An Attune NXT Acoustic Focusing Flow Cytometer was used for all analysis. A BD FACS Aria III was used for cell sorting.
Software	Attune Cytometric Software was used in sample acquisition. Cells were sorted using BD FACSDiva and all flow analysis was performed with FlowJo (v10.8.0; Treestar).

Cell population abundance

Samples were sorted directly into Trizol (for RNA-SEQ) and pure FBS for (ATAC-SEQ). On test sorts with identical panels the cell purity was >95% determined by flow analysis on sorted populations.

Gating strategy

Cells were identified with a FSC-A/SSC-A gate. Next single cells were selected with a FSC-H/FSC-A and a SSC-H/SSC-A gate. Live cells were distinguished based on DAPI staining or Ghost Dye Viability staining (Violet 450 or Red780). Target cells were identified by CD8 and CD90.1 gating for downstream analysis. This gating strategy was used for both cell sorting and analysis and is described in the Extended Data section.

Tick this box to confirm that a figure exemplifying the gating strategy is provided in the Supplementary Information.